Terahertz-Field-Induced Stark Effect in Metal Phthalocyanine Thin Film

Jinying Yang

A thesis

submitted in partial fulfillment of the

requirements for the degree of

Master of Science in Applied Chemical Science and Technology

University of Washington

2026

Committee:

Jiaojian (Tristan) Shi

Dianne J. Xiao

Program Authorized to Offer Degree:

Chemistry

University of Washington

Abstract

Terahertz-Field-Induced Stark Effect in Metal Phthalocyanine Thin Film

Jinying Yang

Chair of the Supervisory Committee:

Jiaojian (Tristan) Shi

Department of Chemistry

Molecular-scale electric-field control is an important direction for future nanoscale switching and information-storage materials. Metal phthalocyanines provide a useful platform for studying molecular electric-field responses because of their chemical stability and tunable molecular structure. In molecular thin films, electric-field control is often reflected in changes in electronic transitions and exciton energies. Meanwhile, these field-induced responses are strongly influenced by intermolecular coupling, molecular packing, and exciton character, and therefore cannot be understood simply as isolated-molecule Stark responses.

Here, we investigate how strong ultrafast terahertz (THz) electric fields modify molecular excitonic responses in metal phthalocyanine thin films using THz-pump optical-probe transient absorption spectroscopy. We observe an anomalous blue-shifting response of the Q-band absorption, in contrast to the conventional redshift expected from a quadratic Stark effect when the excited state is more polarizable than the ground state. By comparing the transient absorption spectrum with the derivatives of the static absorption spectrum, we find that the signal closely resembles the negative first derivative, indicating a field-induced blueshift of the absorption band. We attribute this blueshift to a reduction of the exciton binding energy caused by THz-field-enhanced intermolecular charge-transfer character in stacked metal

phthalocyanine films. This result suggests that field-driven charge separation can overcome the conventional Stark redshift and produce a net transient blueshift in molecular excitonic systems.

TABLE OF CONTENTS

LIST OF FIGURES

LIST OF TABLES

Chapter 1 Introduction

1.1 Motivation

The continuing miniaturization of electronic devices motivates the search for molecular-scale functional materials[1, 2], where individual molecules or molecular assemblies could act as the active unit for information storage or switching[3]. Single-molecule magnets have already shown that magnetic states can be controlled at the molecular level[4, 5], suggesting that other molecular order parameters, such as electric polarization, may also be useful for future nanoscale devices.

In this context, single-molecule ferroelectrics are an attractive long-term goal because switchable electric polarization could potentially enable low-power, stable, and highly integrated molecular memory elements[6]. Metal phthalocyanines are promising model systems for exploring this idea because they are chemically stable, structurally tunable, and contain a central metal ion whose position and electronic environment can influence molecular symmetry, dipolar character, and low-energy vibrational motion[7, 8].

A strong terahertz (THz) pulse provides a unique way to interact with such molecular systems. Its photon energy is much lower than visible electronic transitions, but its electric field can be strong and ultrafast[9]. Therefore, THz excitation can act as a transient electric-field drive for low-energy molecular motion, polarization-related dynamics, or field-induced changes in excitonic states[10].

Although the original motivation was to explore THz switching of single-molecule ferroelectric candidates, an essential first step is to understand how metal phthalocyanine systems respond to strong THz electric fields. This thesis therefore focuses on copper phthalocyanine thin films as a model system and investigates how the THz field modifies the Q-band excitonic response. By studying the transient optical response, molecular packing, and field-induced spectral shifts, this work provides a foundation for understanding electric-field-driven dynamics in metal phthalocyanine materials and for future studies of molecular-scale switching.

1.2 Research Objective and Thesis Overview

The main objective of this thesis is to investigate the static characterization and THz-field-induced optical responses of phthalocyanine thin films, with particular emphasis on the Q-band absorption region. Phthalocyanines exhibit strong visible electronic transitions that are sensitive to molecular packing, aggregation, solvent processing, and film morphology. These properties make them useful molecular systems for studying how in-plane structure influences ultrafast field-driven optical behavior.

This thesis focuses on copper phthalocyanine films, while titanyl phthalocyanine and metal-free phthalocyanine films are also examined as related phthalocyanine systems for comparison. Different sample preparation methods, including toluene processing and trifluoroacetic acid (TFA) processing, are used to modify the thin-film structure and optical response. Static characterization methods, including X-ray diffraction, UV-visible (UV-VIS) absorption spectroscopy, polarization-dependent absorption, and low-wavenumber Raman spectroscopy, are used to establish the structural and optical properties of the prepared films. These measurements provide the equilibrium reference needed to interpret the transient absorption response under THz excitation.

The central goal of this thesis is to determine how a free-space THz pulse modifies the visible absorption spectrum of phthalocyanine thin films. Since the THz photon energy is much lower than the Q-band transition energy, the THz pulse primarily acts as a strong transient electric-field perturbation rather than a resonant electronic excitation. The THz-pump transient absorption measurements are therefore used to examine field-induced changes in the Q-band region, including transient spectral shifts and line-shape changes. Attention is given to the THz-induced transient blue shift observed in copper phthalocyanine films and its possible connection to Stark effect optical responses.

The thesis is organized as follows. Chapter 1 introduces the motivation and research objectives of the work. Chapter 2 provides the theoretical and experimental background necessary for interpreting the results. It begins with the Stark effect, including the general Hamiltonian, first-order and second-order Stark effects, and their connection to transient absorption line shapes. The chapter then introduces the electronic structure of metal phthalocyanines, with emphasis on Q-band transitions, solid-state stacking, Davydov splitting, and the α- and β-form packing structures. The basic principles of terahertz spectroscopy, free-space THz generation, electro-optic

sampling, and transient absorption spectroscopy are also discussed, followed by a summary of previous related work.

Chapter 3 describes the experimental materials and methods. The preparation procedures for toluene-processed and TFA-processed phthalocyanine films are presented first. The chapter then describes the characterization methods used in this work, including X-ray diffraction, static UV-VIS absorption spectroscopy, absorption anisotropy measurements, static low-wavenumber Raman spectroscopy, and THz-pump transient absorption spectroscopy. The optical layouts, measurement procedures, and data processing methods are introduced in this chapter.

Chapter 4 presents experimental results and discussion. The structural characterization section analyzes the X-ray diffraction patterns of the prepared films. The static optical properties section discusses UV-VIS absorption spectra, polarization-dependent absorption anisotropy, and low-wavenumber Raman spectra. These results are then used as a reference for interpreting the THz-pump transient absorption measurements. The final section focuses on the THz-induced transient blue shift observed in the Q-band region and discusses its possible physical origin in terms of field-induced spectral modulation and Stark-like behavior.

Chapter 5 summarizes the main conclusions of the thesis and discusses possible future directions. Overall, this thesis aims to connect sample preparation, molecular packing, equilibrium optical properties, and ultrafast THz-field-induced dynamics in phthalocyanine thin films. This connection provides insight into how strong transient electric fields interact with molecular electronic transitions in organic thin-film materials

Chapter 2 Background

2.1 Stark Effect

The optical response of molecular and low-dimensional materials is highly sensitive to local electric fields, as it can perturb electronic energy levels, modify oscillator strengths, and mix electronic states with different charge distributions. Thus, the Stark effect provides as a highly effective spectroscopic probe for investigating electronic polarization, charge-transfer character, and excitonic state mixing.

2.1.1 General Hamiltonian

Under the electric-dipole approximation, the Hamiltonian can be written as

$$H = H_0 + H',$$

where H_0 is the unperturbed Hamiltonian and

$$H' = -\hat{\boldsymbol{\mu}} \cdot \boldsymbol{E}$$

is the interaction between the electric field $\boldsymbol{E}$ and the electric dipole operator $\hat{\boldsymbol{\mu}}$.

The unperturbed eigenstate is

$$H_0|n^{(0)}\rangle = E_n^{(0)}|n^{(0)}\rangle.$$

For sufficiently weak electric fields, the new energy of state $|n\rangle$ can be expanded perturbatively as

$$E_n = E_n^{(0)} + E_n^{(1)} + E_n^{(2)} + \cdots ,$$

where $E_n^{(1)}$ and $E_n^{(2)}$ are the first- and second-order Stark energy corrections, respectively.

2.1.2 First-order Stark Effect

Due to the non-degenerate perturbation theory, the first-order correction can be written as

$$E_n^{(1)} = \langle n^{(0)}|H'|n^{(0)}\rangle.$$

Substituting the electric dipole perturbation yields

$$E_n^{(1)} = -\langle n^{(0)}| \, \hat{\boldsymbol{\mu}} \cdot \hat{\boldsymbol{E}} \, |n^{(0)}\rangle.$$

By assuming the external field to be classical, the first-order shift can be expressed as:

$$E_n^{(1)} = -\boldsymbol{\mu}_{nn} \cdot \boldsymbol{E},$$

where

$$\boldsymbol{\mu}_{nn} = \langle n^{(0)}| \, \hat{\boldsymbol{\mu}} \, |n^{(0)}\rangle$$

represents the permanent dipole moment of state $|n\rangle$. Thus, the first-order Stark shift exhibits a linear relationship with the applied electric field, arising from the interaction between the permanent dipole moment of the quantum state and the external field.

Given that the optical transition of energy from a ground state $|g\rangle$ to an excited state $|e\rangle$ is

$$E_{eg} = E_e - E_g.$$

So, the first-order shift of the optical transition energy is

$$\Delta E_{eg}^{(1)} = E_e^{(1)} - E_g^{(1)}.$$

Substituting

$$E_e^{(1)} = -\boldsymbol{\mu}_{ee} \cdot \boldsymbol{E}$$

and

$$E_g^{(1)} = -\boldsymbol{\mu}_{gg} \cdot \boldsymbol{E}$$

The first-order shift can be written as

$$\Delta E_{eg}^{(1)} = -\boldsymbol{\mu}_{ee} \cdot \boldsymbol{E} + \boldsymbol{\mu}_{gg} \cdot \boldsymbol{E}$$

Therefore,

$$\Delta E_{eg}^{(1)} = -\Delta\boldsymbol{\mu} \cdot \boldsymbol{E}$$

where

$$\Delta\boldsymbol{\mu} = \boldsymbol{\mu}_{ee} - \boldsymbol{\mu}_{gg}$$

is the difference in permanent dipole moments between the excited state and the ground state.

This result indicates that the linear Stark shift of optical transitions represents the change in permanent dipole moment when excited. When $\Delta\mu = 0$, even if the individual states involved possess intrinsic permanent dipole moment, the transition still does not exhibit a first-order Stark shift. In systems possessing inversion symmetry, the expectation value of the dipole moment operator for quantum states with well-defined parity is typically zero, resulting in the first-order Stark shift being forbidden by symmetry constraints.

2.1.3 Second-order Stark Effect

Due to the non-degenerate perturbation theory, the second-order correction can be written as

$$E_n^{(2)} = \sum_{m\neq n} \frac{\left|\left\langle m^{(0)}\middle|\boldsymbol{H}'\middle|n^{(0)}\right\rangle\right|^2}{E_n^{(0)} - E_m^{(0)}}.$$

Substituting the electric dipole perturbation yields

$$E_n^{(2)} = \sum_{m\neq n} \frac{\left|\left\langle m^{(0)}\middle|\hat{\boldsymbol{\mu}}\cdot\boldsymbol{E}\middle|n^{(0)}\right\rangle\right|^2}{E_n^{(0)} - E_m^{(0)}}.$$

Since this term is quadratic in the electric field, arising from field-induced mixing between state $|n\rangle$ and other states $|m\rangle$, the second-order shift can be written as:

$$E_n^{(2)} = E^2 \sum_{m\neq n} \frac{|\mu_{mn}|^2}{E_n^{(0)} - E_m^{(0)}}$$

where

$$\boldsymbol{\mu}_{mn} = \left\langle m^{(0)}\middle|\,\hat{\boldsymbol{\mu}}\,\middle|n^{(0)}\right\rangle$$

represents the transition dipole moment between state $|n\rangle$ and other states $|m\rangle$.

In tensor notation, the second-order energy shift can be expressed as

$$E_n^{(2)} = -\frac{1}{2}\boldsymbol{E}\cdot\boldsymbol{\alpha}_n\cdot\boldsymbol{E},$$

where

$$\boldsymbol{\alpha}_n = -2 \sum_{m \neq n} \frac{|\mu_{mn}|^2}{E_n^{(0)} - E_m^{(0)}}$$

is the polarizability tensor of state $|n\rangle$. Thus, the second-order Stark shift depends on the dipole coupling between $|n\rangle$ and other states, as well as the energetic separation between them. Nearby states possessing large electric-dipole matrix elements can significantly enhance the polarizability, thereby amplifying the second-order Stark response.

Given the optical transition of energy from a ground state $|g\rangle$ to an excited state $|e\rangle$, the second-order shift of the optical transition energy is

$$\Delta E_{eg}^{(2)} = E_e^{(2)} - E_g^{(2)}.$$

Substituting

$$E_e^{(2)} = -\frac{1}{2} \boldsymbol{E} \cdot \boldsymbol{\alpha}_e \cdot \boldsymbol{E}$$

and

$$E_g^{(2)} = -\frac{1}{2} \boldsymbol{E} \cdot \boldsymbol{\alpha}_g \cdot \boldsymbol{E}$$

The second-order shift can be written as

$$\Delta E_{eg}^{(2)} = -\frac{1}{2} \boldsymbol{E} \cdot \Delta\boldsymbol{\alpha} \cdot \boldsymbol{E}$$

where

$$\Delta\boldsymbol{\alpha} = \boldsymbol{\alpha}_e - \boldsymbol{\alpha}_g$$

is the difference in polarizability between the excited state and the ground state.

Consequently, the quadratic Stark shift shows the change in polarization under photoexcitation, reflecting the field-induced polarization and the virtual coupling to nearby electronic states.

2.1.4 Relation between Stark effect and transient absorption lineshapes

The sign of the transition energy shift induced by the Stark effect determines whether the optical resonance undergoes a red shift or a blue shift. If the unperturbed transition energy is E_0, the field-perturbed transition energy can be written as

$$E_0' = E_0 + \delta E,$$

where δE is the Stark-induced energy shift. A negative shift, $\delta E < 0$, moves the resonance to lower photon energy and therefore corresponds to a red shift, whereas a positive shift, $\delta E > 0$, moves the resonance to higher photon energy and corresponds to a blue shift. Schematic illustrations are shown in Figure 2.1 A and B.

Combining the first- and second-order contributions, the Stark shift of an optical transition can be expressed as

$$\delta E = -\Delta\boldsymbol{\mu} \cdot \boldsymbol{E} - \frac{1}{2}\boldsymbol{E} \cdot \Delta\boldsymbol{\alpha} \cdot \boldsymbol{E} + \cdots.$$

The direction of the spectral shift is determined by the sign of the linear and quadratic Stark terms.

When the linear Stark term dominates, the direction of the spectral shift is determined by the projection of the dipole-moment difference $\Delta\boldsymbol{\mu}$ onto the applied electric field. Specifically,

$$\delta E^{(1)} = -\Delta\boldsymbol{\mu} \cdot \mathbf{E} = -|\Delta\boldsymbol{\mu}||\mathbf{E}|\cos\,\theta,$$

where θ is the angle between $\Delta\boldsymbol{\mu}$ and $\mathbf{E}$. When $\Delta\boldsymbol{\mu} \cdot \mathbf{E} > 0$, which means $\Delta\boldsymbol{\mu}$ has a positive projection along the field direction, the transition energy is lower and produces a red shift. When $\Delta\boldsymbol{\mu} \cdot \mathbf{E} < 0$, a negative projection of $\Delta\boldsymbol{\mu}$ raises the transition energy and produces a blue shift.

For the quadratic Stark contribution, the direction of the quadratic Stark shift is determined by how the polarizability changes upon optical excitation. The second-order shift of an optical transition is

$$\delta E^{(2)} = -\frac{1}{2}\mathbf{E} \cdot \Delta\boldsymbol{\alpha} \cdot \mathbf{E},$$

In a scalar field geometry, this is

$$\delta E^{(2)} = -\frac{1}{2}\Delta\alpha E^2.$$

Since $E^2 > 0$, the sign is determined by the sign of $\Delta\alpha$. When $\Delta\alpha > 0$, the excited state is more polarizable than the ground state, it is stabilized more strongly by the applied electric field. As a result, the positive polarizability difference decreases the transition energy and produces a red shift. When $\Delta\alpha < 0$, the ground state is more

polarizable than the excited state, so the ground state is stabilized more strongly. In this case, the transition energy increases and the resonance blue shifts.

Compared to the linear Stark response, the quadratic Stark response is even in the electric field. Therefore, the quadratic Stark shift does not reverse sign under field reversal.

For sufficiently small shifts, this field-induced displacement produces a derivative-like transient absorption lineshape with respect to the steady-state absorption spectrum[11].

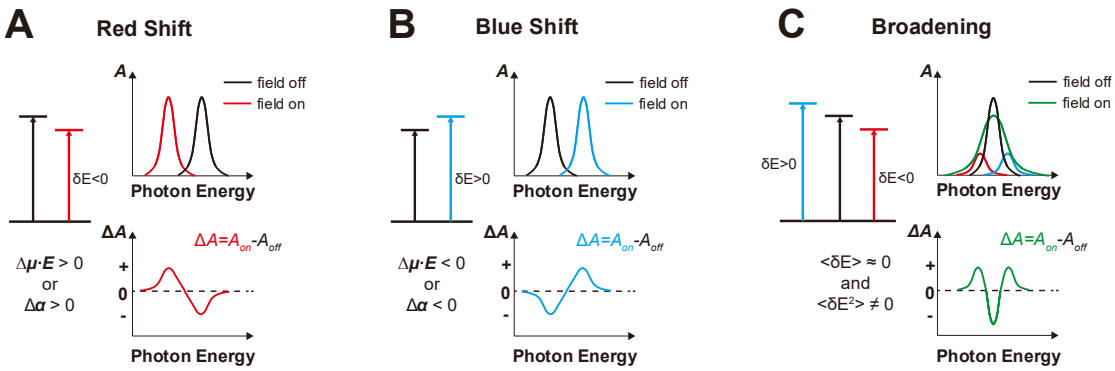

Figure 2.1 Schematic illustration of Stark-effect-induced changes in an absorption lineshape: (A) red shift, (B) blue shift, and (C) spectral broadening.

It should be noted that the experimentally observed Stark lineshape depends not only on the microscopic Stark parameters, but also on ensemble averaging over molecular orientations, domains, and local environments. Therefore, in addition to a uniform red or blue shift, the applied electric field can also induce spectral broadening (Figure 2.1 C). Broadening occurs when different subpopulations experience Stark shifts with different magnitudes or opposite signs, leading to a distribution of transition energies rather than a single shifted resonance. In this case, the average transition energy may remain nearly unchanged, while the variance of the transition-energy distribution increases.

In this situation, the effect of broadening can be understood by averaging over a distribution of local Stark shifts. For a small local transition-energy shift δE, the field-perturbed absorption spectrum can be written as $A(E-\delta E)$. Expanding this expression to second order gives

$$A(E-\delta E) \approx A(E) - \delta E \frac{dA}{dE} + \frac{1}{2}\delta E^2 \frac{d^2A}{dE^2} + \cdots .$$

The measured Stark response is the difference between the field-on and field-off spectra. After averaging over the distribution of local shifts, the absorption change becomes

$$\langle \Delta A(E) \rangle \approx -\langle \delta E \rangle \frac{dA}{dE} + \frac{1}{2} \langle \delta E^2 \rangle \frac{d^2 A}{dE^2} + \cdots .$$

When the average shift is small, $\langle \delta E \rangle \approx 0$, but the distribution has a finite variance, $\langle \delta E^2 \rangle \neq 0$, the Stark spectrum is dominated by a second-derivative-like component. Therefore, Stark-induced broadening often occurs for the linear Stark contribution, as $\delta E^{(1)} = -\Delta \boldsymbol{\mu} \cdot \mathbf{E}$ has opposite signs for subpopulations with $\Delta \boldsymbol{\mu}$ parallel or antiparallel to the applied field. By contrast, the quadratic Stark contribution, which is $\delta E^{(2)} = -1/2\, \mathbf{E} \cdot \Delta \boldsymbol{\alpha} \cdot \mathbf{E}$, is even in the electric field and therefore tends to produce a net red or blue shift, corresponding to a first-derivative-like spectrum. Changes in oscillator strength produces a zeroth-derivative-like contribution to the original absorption spectrum.

2.2 Metal Phthalocyanine

Metal phthalocyanines (MPcs) are a family of planar π-conjugated macrocyclic molecules that have been widely studied as model systems for organic semiconductors, molecular crystals, and optoelectronic materials. Their strong visible absorption, high chemical stability, and tunable molecular structure make them particularly suitable for investigating how electronic transitions respond to external electric fields. Planar MPcs with divalent metal centers provide a high-symmetry system in which the quadratic Stark response can be emphasized.

As discussed above, the Stark shift of optical transition can be written as

$$\delta E = -\Delta \boldsymbol{\mu} \cdot \mathbf{E} - \tfrac{1}{2} \mathbf{E} \cdot \Delta \boldsymbol{\alpha} \cdot \mathbf{E} + \cdots ,$$

where $\Delta \boldsymbol{\mu}$ is the difference in permanent dipole moment between the excited and ground states, and $\Delta \boldsymbol{\alpha}$ is the corresponding difference in polarizability. The linear Stark term is odd in the applied electric field and is related to the change in permanent dipole moment during photoexcitation, while the quadratic Stark term is even in the electric field and reflects the change in polarizability. Therefore, a molecular system with a strongly suppressed permanent dipole moment is desirable for isolating the quadratic Stark contribution.

Metal-free Phthalocyanines (H_2Pc), as shown in Figure 2.2 A, are planar macrocyclic π-conjugated molecules composed of four isoindole units linked by azomethine bridges. Their central macrocyclic core contains a delocalized 18π-electron aromatic system, which gives strong visible absorption and optoelectronic properties. When the two inner hydrogens in the central cavity are replaced by metal ions, MPcs (Figure 2.2 B) are formed[12]. MPcs with a central divalent metal ion, such as copper phthalocyanine (CuPc), zinc phthalocyanine (ZnPc), and nickel phthalocyanine (NiPc), possess a planar, centrosymmetric molecular geometry with high D_{4h} symmetry[13, 14]. In the single molecule, this symmetry causes permanent dipole moments of the ground and optically excited states to vanish, so the linear Stark contribution is expected to be symmetry-forbidden. As a result, the field-induced shift of the optical transition is expected to be dominated by the quadratic Stark effect.

This symmetry distinguishes planar MPcs from lower symmetry phthalocyanine systems. Although H_2Pc is also centrosymmetric in its ideal planar geometry, the two inner N-H bonds lower the molecular symmetry to D_{2h}. It will make the spectral and orientation effects more complex. Additionally, some oxometal phthalocyanine, such as titanyl phthalocyanine (TiOPc)[15], and Vanadyl phthalocyanine (VOPc)[16] in Figure 2.2 C, contain an axial metal-oxo group that distorts the molecular geometry and breaks inversion symmetry. This non-centrosymmetric structure can introduce a permanent out-of-plane dipole moment and make a linear Stark contribution[15, 17]. However, in thin films, the molecular dipoles may be randomly oriented or distributed among different domains, so the linear Stark contribution can be strongly averaged out or even suppressed in the measured macroscopic response.

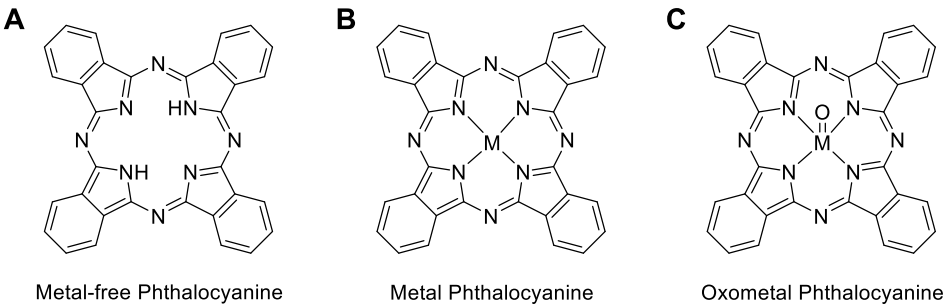

Figure 2.2 Molecular structures of (A) metal-free phthalocyanine, (B) planar metal phthalocyanine (M = Cu, Zn, or Ni) and (C) non-planar oxometal phthalocyanine (M = Ti, or V)

Compared with these lower-symmetry or non-centrosymmetric phthalocyanines, planar MPcs provide a more symmetric and structurally well-defined system to

analyze field-induced optical responses. Under higher symmetry, the permanent dipole moments of both the ground state and the excited states vanish, so the linear Stark contribution is expected to be symmetry-forbidden for an ideal isolated MPc molecule. As a result, the field-induced shift of the optical transition is expected to be dominated by the quadratic Stark effect. The high molecular symmetry, strong visible absorption, and chemical stability of MPcs, especially CuPc, make them useful model systems for connecting the measured Stark response to an effective polarizability difference[18].

2.2.1 Q-band Electronic Structure

MPcs exhibit a distinct characteristic absorption peak in the visible light band, known as the Q-band. This band originates from ligand-centered $\pi \rightarrow \pi^*$ transitions of the phthalocyanine macrocycle. Within the Gouterman four-orbital model[19], these transitions mainly involve excitation from the occupied a_{1u} and a_{2u} type π orbitals to a doubly degenerate unoccupied orbital level of e_g symmetry, which has π^* character[20, 21]. This well-defined optical resonance makes the Q-band a sensitive probe of how the electronic distribution changes under optical excitation and in response to an external electric field.

Among MPcs, CuPc is a particularly useful system for studying field-induced optical responses. CuPc has the planar macrocyclic structure and high molecular symmetry characteristic of divalent MPcs with strong Q-band absorption in the visible region and excellent chemical stability[22], like Figure 2.3.

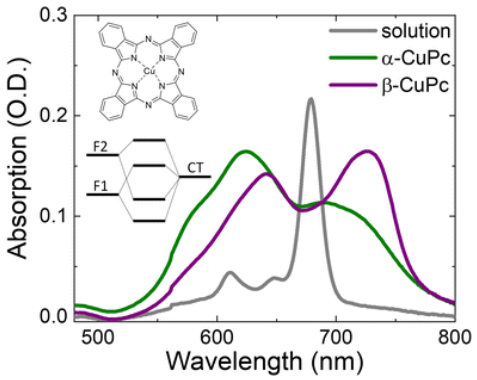

Figure 2.3 Steady-state Q-band absorption spectra of CuPc in solution and thin films. Adapted from the work of del Pino Rosendo et al.[22]

More importantly, in the solid state, CuPc molecules are not isolated. They form ordered or partially ordered molecular assemblies, which provide a useful platform for connecting molecular electronic structure with solid-state effects.

2.2.2 Solid-State Stacking and Polymorphism

Solid-state stacking refers to the way individual CuPc molecules are arranged relative to one another in the film or crystal, including their intermolecular distance, molecular tilt angle, π-π overlap, and relative orientation of transition dipole moments. These structural parameters determine the strength and character of intermolecular electronic interactions. In CuPc films, when neighboring π-conjugated macrocycles are closely packed, their local Q-band excitations can interact through intermolecular excitonic coupling[23]. As a result, the excitation is no longer purely localized on a single molecule, but can form collective exciton states delocalized over neighboring molecules. Therefore, the optical response of a CuPc film is not simply a sum of independent molecular absorptions but is shaped by intermolecular interactions and crystalline packing[22].

Solid CuPc film commonly forms different polymorphs, among which the α- and β-forms are the most common[24]. The emergence of these polymorphs is because planar CuPc macrocycles can pack with different relative translations, slips, tilts, and molecular orientations while maintaining favorable π-π interactions. Therefore, the difference between the α- and β-forms is not a change in the molecular structure of an individual CuPc molecule, but a change in the way neighboring molecules are arranged in the solid state.

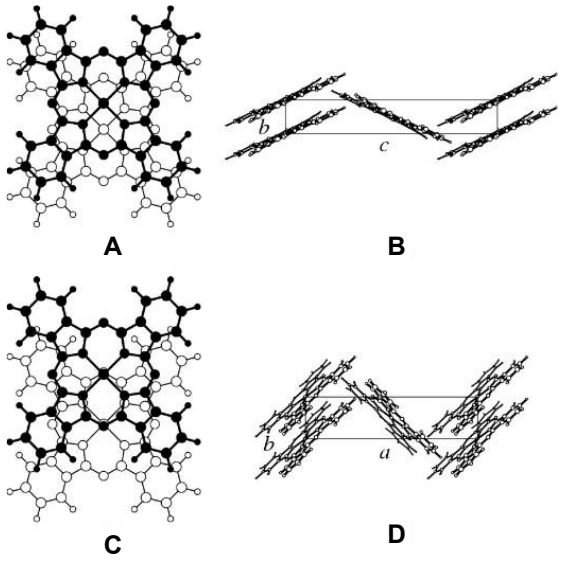

Figure 2.4 Representative crystal packing motifs of planar phthalocyanines. (A) and (B) are α-phase packing. (C) and (D) are β-phase packing. Adapted from the work of Hoshino et al.[25]

Structurally, the α-form is generally regarded as a metastable polymorph, whereas the β-form is often considered the more thermodynamically stable phase. The two phases differ mainly in the relative overlap and displacement between neighboring CuPc molecules. The α-form is commonly associated with a larger overlap between adjacent macrocycles and a shorter intermolecular Cu-Cu separation (Figure 2.4 A and B), while the β-form has a larger relative molecular displacement and a more slipped π-stacked packing arrangement, which is shown as Figure 2.4 C and D[25-27].

As shown in Figure 2.5 A, in the α-form, adjacent molecules within a column overlap more strongly, resulting in a shorter Cu-Cu repeat distance along the molecular stacking direction, commonly reported as approximately 3.79 Å[26-28]. In the β-form (Figure 2.5 B), the CuPc molecules are laterally displaced, and the corresponding Cu-Cu separation along the molecular stack increases to approximately 4.79 Å[26-30]. Although both phases consist of planar CuPc molecules arranged in π-stacked columns, the molecular plane-to-plane separation remains close to 3.4 Å[28, 30]. This difference in molecular slip changes the local packing environment and the directionality of intermolecular interactions.

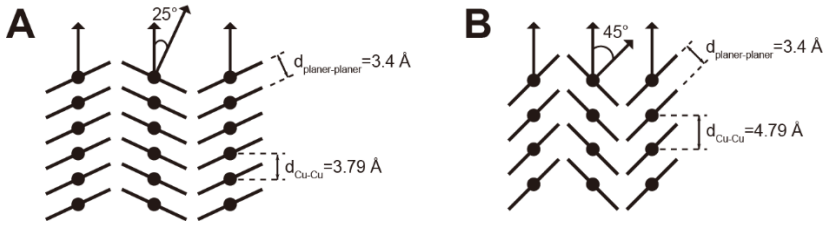

Figure 2.5 Molecular packing geometries of (A) α-form CuPc and (B) β-form CuPc.

The formation of different CuPc polymorphs is strongly affected by preparation conditions[31]. The α-form is commonly obtained under kinetically controlled growth conditions, such as room-temperature deposition[26], where the molecules are trapped in a metastable packing arrangement. In contrast, the β-form is generally regarded as the more thermodynamically stable phase and can be produced by thermal annealing[32] of α-CuPc films or by deposition on heated substrates[33]. Solvent-mediated recrystallization[34] have also been reported to influence CuPc polymorphism. Since the α-form is metastable, it can transform into the more thermodynamically stable β-form upon thermal annealing, high-temperature deposition, or solvent-assisted treatment[26].

These structural parameters represent idealized or average packing geometries, but real CuPc thin films can be more complex. Terms such as herringbone and brickstone describe representative packing motifs of planar CuPc molecules[28]. In herringbone-

like packing, neighboring molecules are tilted relative to each other, whereas in brickstone-like packing, molecules are more nearly parallel and laterally slipped. Figure 2.6[28] illustrates the representative herringbone-like and brickstone-like packing motifs of CuPc molecules. These arrangements change the relative slip and overlap between adjacent π-conjugated macrocycles and provide different packing environments within the film.

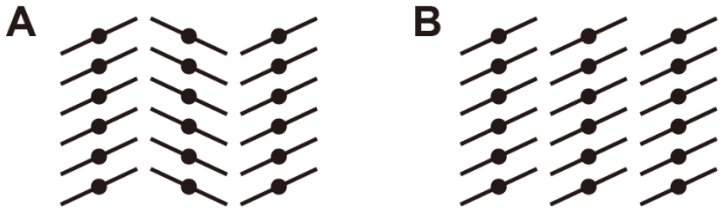

Figure 2.6 Schematic illustration of molecular packing motifs in CuPc thin films. (A) Herringbone-like packing. (B) Brickstone-like packing.

2.2.3 Davydov Splitting and Frenkel-CT Mixing

Based on the solid-state packing discussed above, the optical response of CuPc films cannot be treated simply as a sum of isolated molecular absorptions. Solid-state stacking determines the way individual CuPc molecules are arranged relative to one another in the film or crystal, including their intermolecular distance, molecular tilt angle, π-π overlap, and relative orientation of transition dipole moments. These structural parameters determine the strength and character of intermolecular electronic interactions.

One of the specific manifestations of such excitonic coupling in ordered molecular crystals is called Davydov splitting. In ordered CuPc molecular crystals, if two or more equivalent or nearly equivalent molecules are present in the unit cell, the intermolecular excitonic coupling can split a single molecular Q-band excitation into multiple exciton states with different energies[35, 36], shown as Figure 2.7. As a result, the Q-band in solid CuPc often appears as multiple absorption components rather than a single isolated-molecule transition and its peak positions[37] and intensity ratios that depend sensitively on molecular packing geometry and crystalline polymorphism[23, 38].

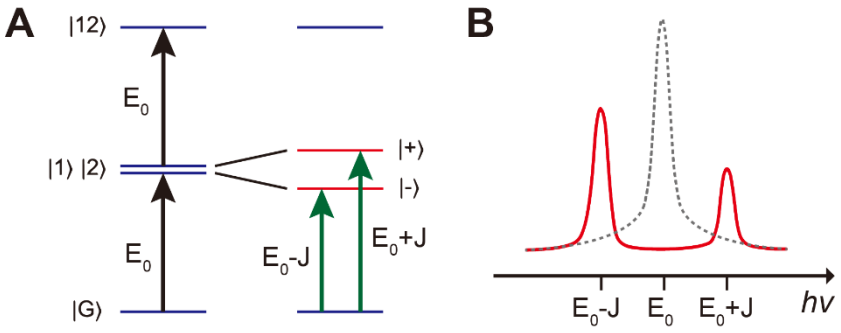

Figure 2.7 Schematic illustration of Davydov splitting of the Q-band transition in stacked CuPc molecules. Two degenerate local excitations, $|1\rangle$ and $|2\rangle$, are coupled by intermolecular excitonic coupling and split into two collective exciton states, $|+\rangle$ and $|-\rangle$, with energies $E_0 + J$ and $E_0 - J$, respectively.

In addition to Davydov splitting, π-stacked CuPc films may also exhibit Frenkel-charge-transfer excitons, or Frenkel-CT mixing excitons[22]. A Frenkel exciton refers to a localized molecular excitation in which the electron and hole remain mainly on the same CuPc molecule. In contrast, an intermolecular charge-transfer exciton involves partial separation of the electron and hole over neighboring molecules, where the electron is transferred to an adjacent molecule while the hole remains on the original molecule[39, 40]. In a π-stacked molecular solid, these two types of excitations can interact because neighboring CuPc macrocycles are close enough for intermolecular electronic coupling[41, 42].

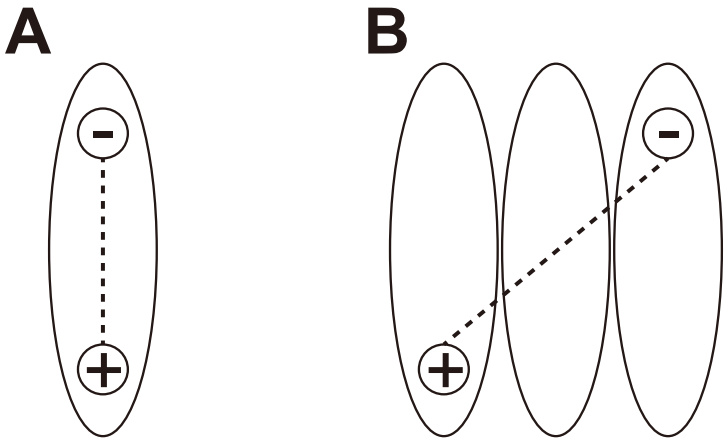

Figure 2.8 Schematic illustration of (A) Frenkel exciton and (B) charge transfer exciton.

Therefore, the Q-band excitation in solid CuPc does not need to be purely Frenkel-like. Instead, it can contain both localized molecular excitation character and intermolecular CT character. This hybridization is referred to as Frenkel-CT mixing[41,

[42]. The degree of mixing depends strongly on molecular packing geometry, intermolecular distance, relative slip, π-π overlap, and crystalline polymorphism. As a result, Frenkel-CT mixing can modify the Q-band peak position, oscillator strength, intensity distribution, and linewidth[22]. It also provides a possible explanation for why the Q-band absorption in CuPc thin films is broader and more structured than that of isolated CuPc molecules in solutions.

This concept is particularly important for interpreting the field-induced optical response of CuPc films. Because CT-like excitonic states involve partial electron-hole separation between neighboring molecules, they are expected to be more sensitive to an external electric field than purely localized molecular excitations[43]. Therefore, an intense THz electric field may perturb the relative energies or mixing between Frenkel and CT exciton states, leading to transient changes in the Q-band absorption[44]. In this sense, the THz-induced spectral shift in solid CuPc should not be interpreted only as a Stark shift of an isolated molecule, but also in the context of intermolecular coupling, π-stacked packing, Davydov splitting, and possible Frenkel-CT mixing.

2.3 Terahertz Radiation

Terahertz (THz) radiation refers to electromagnetic waves in the frequency range between microwaves and the infrared, typically from approximately 0.1 to several THz, corresponding to photon energies on the order of meV[45]. This energy scale is comparable to many low-energy excitations in condensed matter systems, such as phonons, magnons, excitons, free-carrier motion, and collective modes[46]. Therefore, THz spectroscopy provides a powerful way to probe low-energy dynamics that are not easily accessed by conventional optical spectroscopy.

In this thesis, the THz pulse is used primarily as a strong ultrafast electric-field pump rather than as a conventional THz spectroscopic probe. Because the THz photon energy is far below the CuPc Q-band transition energy[45], the THz pulse does not resonantly excite the Q-band absorption. Instead, its oscillating electric field can drive field-induced changes in the molecular thin film. These changes may include Stark-like modulation of excitonic transitions, field-induced charge redistribution, changes in intermolecular charge-transfer character, or coupling to low-energy molecular and lattice motions.

This use of THz excitation is different from conventional optical pumping. A visible or near-infrared pump usually creates real electronic populations by resonantly or

near-resonantly exciting electronic transitions. In contrast, a THz pump mainly acts through its transient electric field and can modify the energy, lineshape, or character of existing excitonic transitions without directly exciting the visible Q-band. This makes THz-pump optical-probe spectroscopy a useful approach for studying ultrafast electric-field-induced responses in molecular excitonic systems.

The following sections describe the generation of free-space THz pulses using tilted-pulse-front optical rectification in $LiNbO_3$, followed by characterization of the THz electric field using electro-optic sampling in a GaP crystal.

2.3.1 Free-space Terahertz Generation

Free-space THz pulses are commonly generated by converting ultrafast optical pulses into electromagnetic radiation at THz frequencies. One widely used mechanism for this conversion is optical rectification, a second-order nonlinear optical process that occurs in non-centrosymmetric media. When an intense femtosecond laser pulse propagates through such a medium, the induced polarization can be expanded as a power series

$$P(t) = \varepsilon_0\left[\chi^{(1)}E(t) + \chi^{(2)}E^2(t) + \chi^{(3)}E^3(t) + \cdots\right],$$

where $\chi^{(1)}$, $\chi^{(2)}$, and $\chi^{(3)}$ are the first-order, second-order, and third-order susceptibilities, respectively. For THz generation by optical rectification, the important term is the second-order nonlinear polarization,

$$P^{(2)}(t) = \varepsilon_0\chi^{(2)}E^2(t).$$

For an ultrashort optical pulse, the electric field can be viewed as a rapidly oscillating carrier modulated by a slowly varying pulse envelope. In a second-order nonlinear medium, the induced polarization contains a term proportional to $E^2(t)$. This term includes both a high-frequency component associated with second-harmonic generation and a low-frequency component that follows the pulse intensity envelope. Since the envelope varies on a femtosecond-to-picosecond timescale, the resulting nonlinear polarization contains THz-frequency components and can radiate a broadband THz field. This process, known as optical rectification, is a widely used method for generating single-cycle and few-cycle THz pulses.

In the present setup, this optical rectification process is implemented in a $LiNbO_3$ crystal. $LiNbO_3$ is commonly used for high-field THz generation because of its large second-order nonlinear coefficient and good efficiency in the low-THz range. However, the THz refractive index of $LiNbO_3$ is much larger than the optical group

index of the pump pulse, producing a large velocity mismatch between the optical pump and the generated THz wave. In a conventional collinear geometry, this mismatch limits the effective interaction length and reduces the THz conversion efficiency.

To overcome this limitation, tilted-pulse-front geometry is used[47, 48], which is shown in Figure 2.9. A diffraction grating introduces angular dispersion to the 1030 nm pump beam, tilting the pulse intensity front relative to the phase front. The tilted pulse front is then imaged into the $LiNbO_3$ crystal[47-49]. The tilt angle is chosen so that the projection of the optical group velocity along the THz propagation direction matches the THz phase velocity, allowing THz radiation generated at different positions in the crystal to add constructively[50].

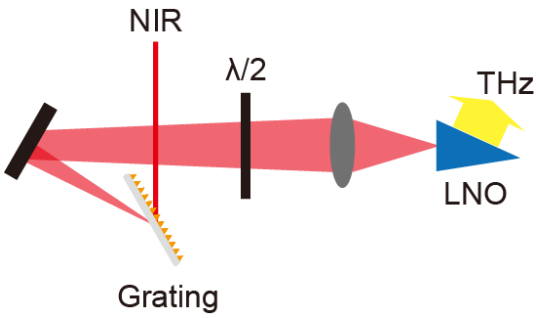

Figure 2.9 Schematic illustration of $LiNbO_3$-based tilted-pulse-front optical rectification for free-space THz generation.

Polarization is also important. In $LiNbO_3$, the largest nonlinear tensor component is commonly associated with d_{33}[51]. Therefore, the pump polarization is usually aligned along with the appropriate crystallographic axis of the $LiNbO_3$ crystal to maximize the nonlinear conversion efficiency. In practice, a half-wave plate can be used before the THz generation stage to rotate the pump polarization into the desired direction[48]. After generation, the THz beam is collected, collimated, and focused using off-axis parabolic mirrors[52]. Because water vapor absorbs strongly in the THz range[53, 54], the THz beam path is often enclosed and purged with dry air or nitrogen.

2.3.2 Electro-Optic Sampling

Electro-optic (EO) sampling is used to measure the temporal trace of the generated THz pulse's electric field. The method is based on the Pockels effect, in which an applied electric field induces a linear change in the refractive index of a non-centrosymmetric crystal[55]. When a THz pulse and a synchronized femtosecond optical probe pulse overlap in an electro-optic crystal, the instantaneous THz electric

field modifies the refractive indices experienced by different polarization components of the probe pulse. This produces a transient birefringence and changes the polarization state of the optical probe. Free-space electro-optic sampling of THz beams is a standard coherent detection method and directly maps the THz-induced birefringence onto an optical polarization change[56].

In this thesis, GaP is used as the EO sampling crystal because of its suitable electro-optic response, near-infrared transparency, and useful detection bandwidth for THz time-domain measurements.[46, 51]. The THz-induced refractive-index change can be written approximately as

$$\Delta n \propto n^3 r E_{THz},$$

where n is the refractive index of the EO crystal, r is the relevant electro-optic coefficient, and E_{THz} is the instantaneous THz electric field. As the optical probe pulse propagates through the GaP crystal, this THz-induced birefringence creates a phase retardation between two orthogonal polarization components of the probe beam:

$$\Delta\phi = \frac{2\pi}{\lambda}\Delta n L,$$

where λ is the probe wavelength and L is the thickness of the EO crystal. For small phase retardation, the induced polarization change is approximately linear in the THz electric field. So the measured EO signal is proportional to $E_{\mathrm{THz}}(t)$, rather than to the THz intensity.

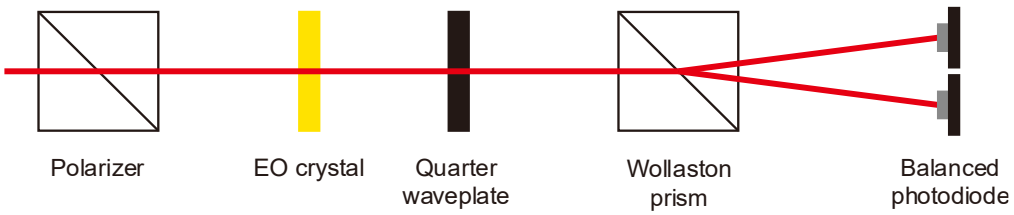

Figure 2.10 Schematic of GaP-based electro-optic sampling for THz electric-field detection.

Experimentally, as before the GaP crystal, a polarizer is used to define a clean linear polarization state of the optical probe pulse, which improves the sensitivity and stability of the subsequent electro-optic detection[56, 57]. Then the THz pulse and the optical probe pulse are spatially overlapped in the GaP crystal, and the relative delay between them is scanned. Since the optical probe pulse is much shorter than the THz waveform, it samples the instantaneous THz field at a specific time delay[58]. By

scanning the delay, the full temporal waveform $E_{\mathrm{THz}}(t)$can be reconstructed point by point[46, 55].

After passing through the GaP crystal, the probe polarization is analyzed using a quarter waveplate, a Wollaston prism, and a balanced photodetector[48, 50]. The quarter waveplate converts the THz-induced ellipticity or polarization rotation into an intensity imbalance between two orthogonal polarization components. The Wollaston prism separates these two components, and the balanced photodiode measures their difference. For small EO modulation, the normalized balanced signal can be written as

$$\frac{I1-I2}{I1+I2} \propto \Delta\phi \propto E_{THz}(t).$$

Thus, the balanced photodiode output is directly proportional to the instantaneous THz electric field. Recording this signal as a function of pump-probe delay gives the time-domain THz waveform.

The bandwidth and sensitivity of EO sampling depend on the probe pulse duration, EO crystal thickness, phase matching between the optical and THz pulses, THz absorption, and phonon resonances of the EO crystal[59]. A thicker GaP crystal generally provides a stronger signal because the probe accumulates more phase retardation, but it can reduce the high-frequency detection bandwidth due to velocity mismatch and dispersion[59, 60]. Therefore, the choice of GaP thickness represents a trade-off between detection sensitivity and bandwidth.

In summary, the THz setup used in this thesis combines tilted-pulse-front optical rectification in $LiNbO_3$ for THz generation with electro-optic sampling in GaP for field-resolved THz detection. This approach provides direct access to the temporal profile and spectral content of the THz electric field, which is essential for interpreting THz-driven ultrafast material responses.

2.4 Transient Absorption Spectroscopy

Transient absorption spectroscopy is a time-resolved optical technique used to monitor how the absorption spectrum of a material evolves after an external excitation. Its conceptual origin can be traced back to flash photolysis, in which a short light pulse was used to initiate a photochemical reaction and a delayed probe was used to detect transient species. With the development of pulsed lasers,

femtosecond laser sources, optical parametric amplifiers, and broadband white-light detection, this approach has been extended from microsecond and nanosecond photochemistry to ultrafast dynamics on femtosecond-to-picosecond time scales.

In modern implementations, transient absorption spectroscopy is commonly performed in a pump-probe geometry: an excitation pulse perturbs the sample, and a time-delayed probe pulse measures the resulting pump-induced change in optical absorption. As a result, transient absorption has become one of the central techniques for studying non-equilibrium dynamics in molecules, semiconductors, nanomaterials, and correlated condensed-matter systems.

Compared with static absorption spectroscopy, transient absorption spectroscopy provides a non-equilibrium perspective on the optical properties of materials. Static absorption measurements reveal the equilibrium electronic or vibrational structure of a sample, but they do not directly show how the absorption spectrum evolves after the system is driven away from equilibrium. Transient absorption spectroscopy fills this gap by tracking the time-dependent change in optical density, usually expressed as ΔOD or ΔA, after photoexcitation or field excitation. This allows the temporal evolution of absorption features, spectral shifts, linewidth changes, ground-state bleaching, excited-state absorption, stimulated emission, and other transient responses to be monitored directly. More importantly, the ultrafast time resolution of transient absorption makes it possible to resolve intermediate processes that are hidden in steady-state spectra, including carrier cooling, exciton formation and relaxation, charge transfer, energy transfer, spin-state evolution, lattice relaxation, and other coupled electronic, spin, or structural dynamics. Therefore, transient absorption spectroscopy is not only a method for measuring excited-state lifetimes, but also a powerful tool for revealing the pathways through which energy is redistributed and transferred among different degrees of freedom in a material.

Experimentally, a typical transient absorption setup divides an ultrafast laser output into pump and probe arms. The pump pulse is used to excite or perturb the sample, while the probe pulse interrogates the sample after a controlled time delay. The delay between the pump and probe pulses is usually adjusted by a mechanical translation stage or an electronic timing system. Specifically, other than other types of transient optical measurement, transient absorption often uses broad-band white light (usually generated by white light crystal such as Al_2O_3 or YAG crystals) as probe beam to capture the spectal information.

However, since transient absorption focus not only time-resolved but also frequency-resolved non-equilibrium changes, the signals is often extremely smaller even than typical ultarfast detection. Thus, sensitive detection schemes are essential. In one common approach, the pump beam is modulated by an optical chopper, and the pump-induced signal is extracted using a lock-in amplifier while the probe spectrum is recorded by a spectrometer. This lock-in-based detection scheme greatly suppresses noise that is not synchronized with the pump modulation. In broadband or high-repetition-rate measurements, the detector can also be externally triggered so that pump-on and pump-off probe spectra are recorded in a shot-to-shot or single-shot manner using a CCD, CMOS, or line-scan camera. By directly referencing adjacent or synchronized spectra, this method reduces laser fluctuation noise and improves the sensitivity of the measurement. These detection strategies significantly enhance the signal-to-noise ratio and make it possible to observe very weak pump-induced absorption changes, such as OD=4.

2.5 Previous Works

In many classic Stark-effect studies, the field-induced response of an excitonic or molecular transition was first understood in terms of a red shift. For example, in semiconductor quantum wells, Miller's lab studied the electric-field dependence of optical absorption near the band gap of GaAs/AlGaAs quantum-well structures[61]. When an electric field was applied perpendicular to the quantum-well layers, the confinement potential was tilted, the electron and hole wavefunctions were displaced in opposite directions, and the excitonic absorption shifted to lower photon energy. This work established the conventional picture of the quantum-confined Stark effect, in which the applied field reduces the electron-hole transition energy and produces a red-shifted absorption edge.

Optical Stark experiments also commonly show the red-shifted excitonic resonances depending on the nature of the virtual state involved. Hulin and Joffre reported an excitonic optical Stark redshift in CuCl under below-gap optical excitation[62]. In contrast to the usual optical Stark blueshift expected from simple exciton-photon level repulsion, they attributed the redshift to virtual biexciton formation. In this case, the optical field couples the exciton to a bound two-exciton state, and the biexcitonic contribution reverses the sign of the optical Stark shift. This result shows that even

within optical Stark spectroscopy, the direction of the energy shift depends sensitively on the excitonic many-body states involved.

A similar red-shifting Stark response has also been observed in molecular systems. A classic Stark study of porphyrins by Malley showed an external electric field shifted the porphyrin absorption bands to lower energy[63]. This behavior can be understood as a quadratic Stark effect, where the excited state is more strongly stabilized by the electric field than the ground state because of a change in polarizability upon excitation. As a result, the transition energy decreases under the applied field, giving a red-shifted absorption feature.

In addition to red-shifted Stark responses, field-induced broadening is also a common feature in electro absorption and THz-Stark spectroscopy. For example, Yamanaka studied InP-based quantum wells with strong and weak quantum confinement and showed that an applied electric field can broaden the optical absorption edge rather than simply shift it[64]. This behavior was attributed to field-induced distortion of the confined electron and hole wavefunctions, especially in weakly confined quantum wells, where carrier leakage and reduced confinement smear out the excitonic absorption feature.

Similarly, Singh group reported a transient THz Stark effect in polar liquids, where intense picosecond THz fields induced broadening of the molecular absorption band[65]. In that case, molecules with different orientations experienced Stark shifts of different signs, and the orientational average produced a broadened absorption profile rather than a uniform redshift or blueshift.

Field-induced broadening has also been observed in molecular aggregates. In porphyrin J-aggregates, Nakata lab showed that the electro-optic response can arise from field-induced molecular rearrangement and changes in intermolecular excitonic coupling[66]. Depending on aggregate orientation, the J-band can contain both red-shift-like and blue-shift-like components, which appear as broadening in randomly oriented solutions.

Although the conventional Stark response of an excitonic transition is often associated with a red shift or broadening, previous studies have shown that field-induced blueshifts can also occur through several distinct mechanisms. One representative example is the quantum-confined Stark effect (QCSE), in layered hybrid perovskites reported by Walters[67]. In conventional quantum wells, an applied electric field reduces the electron-hole transition energy and typically produces a red-shifted

excitonic absorption. However, Walters observed an anomalous blue-shifting QCSE in methylammonium-containing layered perovskites. This behavior was attributed to the orientational polarizability of confined methylammonium dipoles: under an applied electric field, the dipolar cations reorient and enhance the spatial separation of the electron and hole wavefunctions. This strongly reduces the exciton binding energy. Since the exciton absorption energy can be written approximately as $E_{abs} = E_{gap} - E_{binding}$, a sufficiently large decrease in binding energy can overcome the field-induced bandgap lowering and produce a net blueshift of the excitonic transition. In contrast, analogous cesium-containing layered perovskites, which lack such orientable molecular dipoles, show the more conventional red-shifting QCSE.

A different route to field-induced blueshift has been demonstrated in polar III-nitride quantum structures. Sari group reported blue InGaN/GaN quantum electro absorption modulators based on a reversed QCSE[68]. In these structures, growth on the polar *c*-plane leads to strong internal polarization fields and a zigzag quantum-well potential profile. The optical transition is therefore already red-shifted by the built-in polarization field at zero or low applied bias. When an external reverse bias is applied in the opposite direction, it partially compensates for the internal polarization field, flattens the quantum-well potential, increases the electron-hole transition energy, and shifts the absorption edge to higher energy. Thus, the observed blueshift does not arise because the external electric field intrinsically raises the transition energy; rather, it occurs because the applied field reduces a pre-existing QCSE caused by the built-in polarization field.

A similar compensation mechanism was recently reported in a two-dimensional semiconductor by Hiraoka, who used a hybrid THz nanoantenna to convert an incident THz pulse into an ultrafast out-of-plane gating field in few-layer MoS_2[69]. The THz field produced coherent Stark shifts of the A- and B-exciton resonances. In an ideal two-dimensional semiconductor without out-of-plane symmetry breaking, the quadratic QCSE would lead to a red shift for either polarity of the applied field. However, their devices contained a built-in out-of-plane electric field, likely associated with asymmetric charged trap states at the MoS_2/oxide interfaces. Depending on its polarity, the THz gating field could either weaken or enhance this pre-existing QCSE. When the THz field opposed the built-in field, the total field magnitude decreased and the exciton resonance shifted to higher energy, giving a transient blueshift; when the THz field reinforced the built-in field, a redshift was observed.

Near-resonant optical Stark effects in monolayer WS_2 provide a further example. Cunningham showed that when the pump is tuned close to the A-exciton resonance, the simple two-level dressed-atom picture is insufficient[70]. In this regime, many-body Coulomb interactions between virtual excitons become important. These exciton-exciton interactions are repulsive and can produce a dominant blueshift even when the pump is tuned above the exciton resonance, as long as the detuning is smaller than the exciton binding energy. This result illustrates that, in strongly bound low-dimensional excitonic systems, optical Stark blueshifts can originate not only from exciton-photon level repulsion but also from many-body exciton-exciton repulsion.

System	Observed response	Mechanism
GaAs/AlGaAs quantum wells[61]	Redshift	Tilt the quantum-well potential and lower the electron-hole transition energy.
CuCl[62]	Redshift	Invoke virtual biexciton formation to reverse the usual optical Stark shift direction.
Porphyrins[63]	Redshift	Stabilize the excited state more strongly than the ground state through the quadratic Stark effect.
InP-based quantum wells[64]	Broadening	Distort the confined electron and hole wavefunctions to broaden the absorption edge.
Polar liquids[65]	Broadening	Average over orientation-dependent Stark shifts to produce spectral broadening.
Porphyrin J-aggregates[66]	Broadening	Modify molecular arrangement and intermolecular excitonic coupling to generate mixed red- and blue-shift-like components.
layered perovskites[67]	Blueshift	Reorient methylammonium dipoles to increase electron-hole separation and reduce exciton binding energy.
InGaN/GaN quantum structures[68]	Blueshift	Compensate the built-in polarization field to reduce the pre-existing QCSE and blueshift the absorption edge.
Few-layer MoS_2[69]	Blueshift	Enhance or compensate the built-in out-of-plane field to produce polarity-dependent blueshifts.

Monolayer WS_2[70]	Blueshift	Use many-body exciton-exciton repulsion to dominate the near-resonant optical Stark response and produce a blueshift.

Table 2.1 Comparison of Stark-Induced Redshift, Broadening, and Blueshift Mechanisms.

Chapter 3 Experimental Materials and Methods

This chapter describes the experimental procedures and characterization methods employed in this work. The main purpose is to document how the samples were prepared, how their structural and optical properties were characterized, and how the ultrafast transient measurements were performed. By providing these details, this chapter establishes the experimental basis for the analysis and discussion of the results in the following chapter.

3.1 Sample Preparation

H_2Pc, TiOPc, and CuPc used in this study were purchased from Millipore Sigma and used without further purification unless otherwise noted.

3.1.1 Toluene-Processed Phthalocyanine Films

Toluene-processed phthalocyanine films were prepared by a drop-casting method using H_2Pc, TiOPc, and CuPc. Two different material loadings were used depending on the intended characterization method. For transmission-based optical measurements, including static UV-VIS absorption, X-ray diffraction and THz-pump transient absorption spectroscopy, 2 mg of each phthalocyanine powder was weighed and transferred into a clean glass vial. Approximately 2 mL of toluene was then added to each vial, giving a nominal mass concentration of 1 mg/mL. For low-wavenumber Raman, a higher material loading was used to obtain thicker deposited films. In this case, 10 mg of each phthalocyanine powder was dispersed in 2 mL of toluene, corresponding to a nominal mass concentration of 5 mg/mL. The mixture was sonicated at room temperature, approximately 18 °C, for 30 min to promote dispersion of the phthalocyanine powder in toluene.

Material	Relative molecular mass (g/mol)	Amount of 2mg (mmol)	Amount of 10mg (mmol)
H_2Pc	514.5	0.0039	0.019
TiOPc	576.4	0.0035	0.017
CuPc	576.1	0.0035	0.017

Table 3.1 Molecular weights and corresponding molar amounts of phthalocyanine powders used for toluene-processed film preparation.

Because phthalocyanines have limited solubility in toluene[71], the prepared mixtures were treated as dispersions rather than completely dissolved molecular solutions.

After sonication, the dispersions were immediately deposited onto different substrates according to the requirements of each characterization method.

For static UV-VIS absorption and THz-pump transient absorption spectroscopy, thin-film samples were prepared on 0.1-mm-thick quartz microslides. These measurements were performed in transmission geometry, so the deposited films needed to be sufficiently thin and continuous to allow light transmission through the sample. A small volume of the phthalocyanine dispersion was first placed near one edge of the microslides. The tip of the disposable dropper was then used to guide the liquid across the microslide surface in one direction. During this process, the dropper tip was kept close to the microslide surface and in contact with the liquid, allowing the dispersion to spread into a thin wet layer over the active area. This spreading step helped distribute the phthalocyanine material over a larger area and reduced the formation of thick localized droplets.

For low-wavenumber Raman, the samples were prepared on 1-mm-thick quartz microslides. Since the Raman measurements were performed in reflection geometry, optical transmission through the film was not required. In this case, the phthalocyanine dispersion was directly drop-cast onto the microslides without the spreading step used for the transmission samples. This produced a thicker deposited layer, which was preferred for obtaining a stronger Raman signal.

For X-ray diffraction, the samples were prepared on silicon substrates using a procedure which is used for the thin-film transmission samples. A small volume of the phthalocyanine dispersion was deposited near one edge of the silicon substrate and then gently spread across the surface with the tip of the disposable dropper. This produced a thin and laterally extended film rather than a thick localized deposit. The thin-film geometry helped improve the uniformity of the illuminated measurement area, while the silicon substrate provided suitable support for structural characterization by X-ray diffraction.

After deposition, the post-deposition treatment depended on the intended characterization method. Samples prepared for static UV-VIS absorption, optical anisotropy measurements, low-wavenumber Raman spectroscopy, and THz-pump transient absorption spectroscopy were thermally treated at 200 °C for 3 h. For X-ray diffraction measurements, two sets of samples were prepared to compare the effect of thermal treatment on the film structure. One set was dried naturally in a fume hood for 3 h at room temperature and is referred to as the as-dried sample. The other set was thermally treated at 200 °C for 3 h.

After drying or thermal treatment, phthalocyanine films were obtained on the corresponding substrates. The H_2Pc, TiOPc, and CuPc films showed characteristic bluish gray, light grayish cyan, and bright blue colors, respectively. A small number of aggregated regions were observed in some areas, which is consistent with the limited solubility of the phthalocyanine powders in toluene. However, the overall film coverage was sufficient for the optical, Raman, X-ray diffraction, and THz-pump transient absorption measurements described in this work.

3.1.2 TFA-Processed Phthalocyanine Films

TFA-treated phthalocyanine films were prepared using a procedure which is similar to the toluene-based drop-casting method, but trifluoroacetic acid (TFA) was used as the processing solvent. This preparation route was applied only to CuPc and TiOPc. H_2Pc was not included in the TFA-treated sample set because the addition of TFA led to pronounced aggregation under the same preparation conditions, producing films that were not suitable for the intended optical measurements. This behavior is likely related to the acid sensitivity of metal-free phthalocyanines and the strong tendency of planar phthalocyanine molecules to undergo π-π stacking and self-association. Previous studies have shown that protonation can significantly modify the electronic structure and aggregation behavior of phthalocyanines, and acid treatment of metal-free phthalocyanine systems may also lead to degradation rather than a stable protonated molecular solution[72, 73].

For CuPc and TiOPc, 2 mg of the corresponding phthalocyanine powder was weighed and transferred into a clean glass vial. Approximately 2 mL of TFA was then added to each vial using a disposable dropper, giving a nominal mass concentration of 1 mg/mL. Upon addition of TFA, both CuPc and TiOPc dissolved completely and formed visually homogeneous solutions. The solutions were then sonicated at room temperature, approximately 18 °C, for 30 min to break up any remaining small aggregates and improve solution uniformity. After sonication, the solutions were centrifuged at 1600 rpm for 10 min. The supernatant was collected and used for film preparation.

Material	Relative molecular mass (g/mol)	Amount of 2mg (mmol)
TiOPc	576.4	0.0035
CuPc	576.1	0.0035

Table 3.2 Molecular weights and corresponding molar amounts of phthalocyanine powders used for TFA-processed film preparation.

For static UV-VIS absorption and THz-pump transient absorption spectroscopy, in addition to the films prepared immediately after solution processing, an additional CuPc/TFA solution was prepared using the same procedure. After centrifugation, the clear supernatant was transferred to a clean vial and stored until detect. The CuPc/TFA and TiOPc/TFA thin-film samples were fabricated on 0.1-mm-thick quartz microslides. Since both measurements were carried out in transmission geometry, the films were required to be thin enough for light transmission while still maintaining continuous sample coverage. A small amount of the CuPc/TFA or TiOPc/TFA solution was deposited near one edge of the quartz microslide. The solution was then slowly drawn across the substrate surface with the tip of the disposable dropper to form a thin liquid layer over the active region. During this step, the dropper tip was kept close to the substrate and remained in contact with the liquid, allowing the solution to spread smoothly across the surface. This procedure helped distribute the phthalocyanine material over a wider area and minimized the formation of thick, localized deposits.

For X-ray diffraction, CuPc/TFA samples were prepared on silicon substrates using a similar thin-film deposition procedure. A small volume of the CuPc/TFA solution was deposited near one edge of the silicon substrate and then gently spread across the surface with the tip of the disposable dropper. This produced a thin and laterally extended film rather than a thick localized deposit. The thin-film geometry helped improve the uniformity of the measurement area, while the silicon substrate provided a suitable support for structural characterization by X-ray diffraction. TiOPc/TFA samples were not prepared for X-ray diffraction measurements in this work.

After deposition, the post-deposition treatment also depended on the intended characterization method. The CuPc/TFA and TiOPc/TFA thin-film samples prepared on 0.1-mm-thick quartz microslides for static UV-VIS absorption and THz-pump transient absorption spectroscopy were thermally treated at 200 °C for 3 h. For X-ray diffraction measurements, CuPc/TFA samples were prepared as two sets to compare the effect of thermal treatment on the film structure. One set was dried naturally in a fume hood for 3 h at room temperature and is referred to as the as-dried sample. The other set was thermally treated at 200 °C for 3 h.

After drying or thermal treatment, TFA-treated phthalocyanine films were obtained on the corresponding substrates. The resulting CuPc/TFA films showed a blue appearance, while the TiOPc/TFA films showed a turquoise appearance. A small number of aggregated regions were observed in some areas, reflecting the sensitivity of phthalocyanine film formation to strongly acidic processing conditions.

Nevertheless, the CuPc/TFA and TiOPc/TFA films prepared on 0.1-mm-thick quartz microslides provided sufficient coverage for static UV-VIS absorption and THz-pump transient absorption measurements, and the CuPc/TFA films prepared on silicon substrates were suitable for X-ray diffraction characterization.

3.2 X-ray Diffraction Characterization

X-ray diffraction measurements were carried out using a Bruker D2 PHASER powder X-ray diffractometer. The measurements were performed on CuPc/TFA and CuPc/toluene samples deposited on silicon substrates. For each solvent-treated condition, both heated and unheated samples were measured in order to evaluate the influence of thermal treatment on the crystalline structure and molecular packing. Each sample condition was measured three times to improve reliability and reduce the influence of random impurity peaks or instrumental artifacts.

The prepared samples were placed on the sample holder and loaded into the diffractometer chamber. After the chamber door was closed and the safety interlock was engaged, the scan parameters were set using the instrument control software. Diffraction patterns were collected over a 2θ range of 3° to 40°, with a step size of 0.05°, a counting time of 1 s per step, and a total scan time of approximately 12 min for each measurement.

After data collection, the diffraction patterns from repeated measurements were compared to identify reproducible diffraction features and to exclude non-reproducible peaks. For each identified diffraction peak, the peak angle, corresponding d-spacing, and relative intensity were analyzed. These parameters were then used to compare the crystallinity, preferred molecular packing, and possible structural differences between the CuPc/TFA and CuPc/toluene samples under heated and unheated preparation conditions.

3.3 Static UV-VIS Absorption

Static UV-VIS absorption spectra were measured using a home-built transmission optical setup, as schematically illustrated in Figure 3.1. The broadband light from a lamp source first passed through a polarizer to define the incident polarization state. The light was then focused on the sample using a focusing lens. After passing through

the sample, the transmitted light was collected by another focusing lens and coupled through a confocal filtering section consisting of two confocal lenses and an iris. The iris was used to spatially filter the transmitted beam and reduce the contribution from scattered or out-of-focus light. After the confocal filtering section, the beam was redirected by a mirror and focused into the entrance of a spectrometer for spectral acquisition.

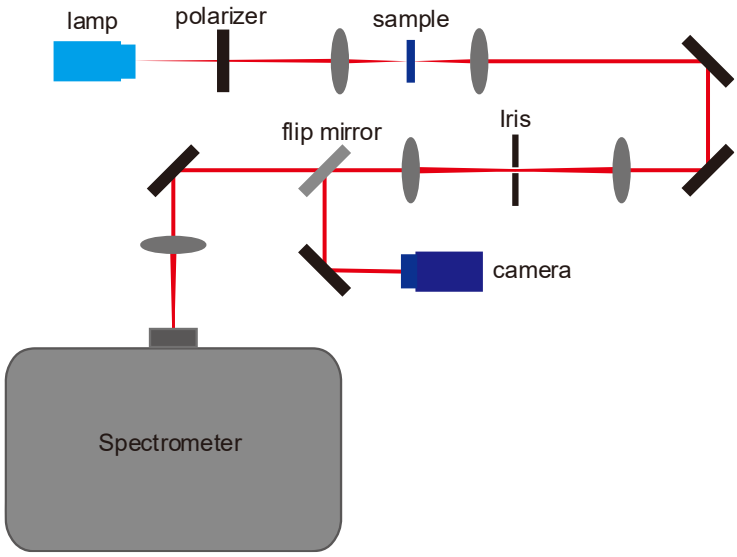

Figure 3.1 Schematic illustration of the home-built static UV-VIS absorption setup.

An imaging path was incorporated into the setup to help locate the sample position and optimize the focus. This imaging system was placed after the confocal lens section and before the mirror leading to the spectrometer. It consisted of a flip mirror and a camera. During alignment, the sample was first mounted in the beam path, and the flip mirror was inserted to direct the image of the sample region onto the camera. The sample position and focus were then adjusted using the imaging system. After the sample focus was optimized, the flip mirror was removed from the beam path, and the transmitted light was directed into the spectrometer for absorption measurements.

The spectra were collected over a wavelength range of 350-1100 nm. For solid-state measurements, thin-film samples were prepared on 0.1-mm-thick quartz microslides. The measured solid samples included H_2Pc/toluene, TiOPc/TFA, TiOPc/toluene, CuPc/TFA and CuPc/toluene films. A clean 0.1-mm-thick quartz microslide was measured as the background reference for these solid-film measurements. For solution measurements, the CuPc/TFA solution was loaded into a cuvette and measured in transmission geometry. An empty cuvette was measured as the corresponding background reference.

For each sample, the background spectrum was measured under the same optical configuration as the sample spectrum. This procedure minimized the influence of the lamp spectrum, substrate or cuvette transmission, and wavelength-dependent response of the optical system and spectrometer. The optical density was calculated from the transmitted sample and reference spectra according to

$$\mathrm{OD}(\lambda) = -\log_{10}\left[\frac{I_{\mathrm{sample}}(\lambda)}{I_{\mathrm{ref}}(\lambda)}\right],$$

where $I_{\mathrm{sample}}(\lambda)$ is the transmitted spectrum through the sample and $I_{\mathrm{ref}}(\lambda)$ is the corresponding background spectrum measured through the blank quartz microslide or empty cuvette. After the optical density spectrum was obtained, each spectrum was normalized by setting its maximum absorption peak to 1 and scaling the remaining spectrum by the same factor. This normalization enabled direct comparison of relative peak positions and spectral line shapes among different samples, while reducing the influence of variations in film thickness, sample coverage, and absolute signal intensity.

Polarization-dependent UV-VIS absorption measurements were also performed to evaluate the optical anisotropy of the CuPc/TFA and CuPc/toluene film samples. During these measurements, the incident polarization direction was controlled by rotating the polarizer. Starting from 0°, absorption spectra were collected every 10° over a full circle rotation, giving a total of 36 spectra for each sample.

For each polarization angle, the optical density spectrum was first calculated using the corresponding background reference. The analysis focused on the right-side peak of the Q-band. To quantify the absorption intensity at this feature, the spectral area was integrated within a ±10 nm wavelength window around the peak position. The integrated Q-band intensity was then plotted as a function of the polarizer angle in a polar plot, with the angular coordinate representing the incident polarization angle and the radial coordinate representing the integrated absorption area.

The polarization anisotropy factor was calculated according to

$$R = \frac{A_{\parallel} - A_{\perp}}{A_{\parallel} + 2A_{\perp}},$$

where $A_{\parallel}$ and $A_{\perp}$ represent the integrated Q-band absorption intensities measured parallel and perpendicular to the principal absorption direction, respectively. This factor was used to quantify the polarization dependence of the Q-band absorption and to compare the degree of optical anisotropy among different thin-film samples.

Overall, the static UV-VIS absorption spectra provided both the spectral absorption features and the polarization-dependent optical response of the prepared phthalocyanine samples. The normalized absorption spectra were used to compare peak positions and line shapes among different samples, while the polarization-dependent measurements and anisotropy factor analysis were used to evaluate the degree of optical anisotropy in thin films. These results provide the necessary static optical reference for interpreting the subsequent THz-pump transient absorption measurements.

3.4 Static Low-wavenumber Raman

The home-built Raman spectroscopy setup used in this work is schematically illustrated in Figure 3.2. A continuous-wave 532 nm laser was used as an excitation source. The laser beam first passed through a lens pair that served as a beam expander, increasing the beam diameter and improving the beam collimation before it entered the microscope optical path. The expanded 532 nm beam was then directed toward the microscope objective and focused onto the sample surface to excite Raman scattering.

After the beam splitter and before the objective, a flip mirror, lamp illumination path, and camera imaging path were integrated into the setup for sample alignment and focusing. The broadband lamp provided white-light illumination of the sample through the same objective, while the reflected image was routed to the camera to locate the sample region and optimize the focus before spectral acquisition.

The Raman signal was collected in a back-scattering geometry with the same objective. After being separated from the excitation path, the collected light passed through a set of 532 nm notch filters to suppress the Rayleigh-scattered laser light. The remaining Raman-scattered light was then focused through an iris, which acted as a spatial filter in the confocal collection path. Finally, the output beam is coupled into a high-resolution spectrometer for low wavenumber Raman spectral acquisition.

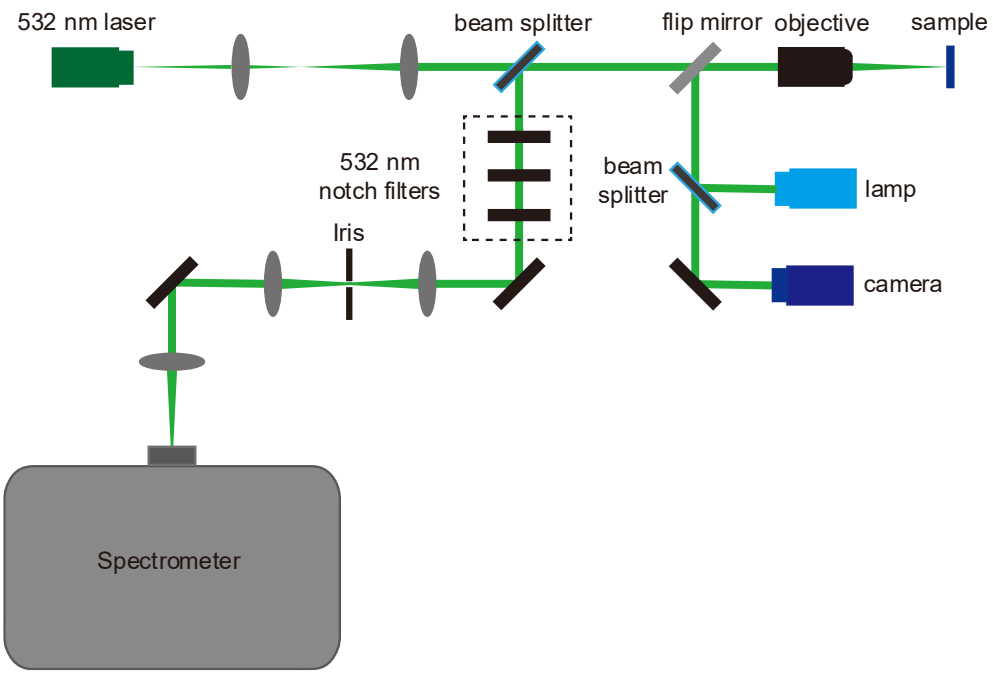

Figure 3.2 Schematic illustration of the home-built low-wavenumber Raman spectroscopy setup.

The measurements were performed on three toluene-prepared thin-film samples: H_2Pc/toluene, TiOPc/toluene, and CuPc/toluene. The detected wavelength was converted to Raman shift according to

$$\Delta\tilde{\nu}\ (\mathrm{cm}^{-1}) = 10^7 \left(\frac{1}{\lambda_{\mathrm{exc}}(\mathrm{nm})} - \frac{1}{\lambda_{\mathrm{Raman}}(\mathrm{nm})}\right),$$

where λ_{exc} is the excitation wavelength and λ_{raman} is the detected Raman-scattered wavelength. For the 532 nm excitation used in this work, λ_{exc} = 532 nm. Based on the excitation wavelength and the accessible spectral window of the detection system, the low-wavenumber Raman range was approximately 5-450 cm^{-1}. The Raman spectra were plotted with Raman shift, in cm^{-1}, as the horizontal axis and intensity, in arbitrary units, as the vertical axis. These spectra were used to examine low-frequency vibrational features of the phthalocyanine films and to compare the Raman-active modes among different molecular systems.

3.5 THz-pump Transient Absorption

The THz-pump transient absorption setup is schematically illustrated in Figure 3.3. The 1030 nm Yb-based picosecond laser provided two output beams. One beam with 500 fs pulse duration was used to generate the THz pump pulse from the fundamental

1030 nm light, while the other beam was first compressed down from 10 ps to about 700 fs and then used to generate a broadband white-light probe for transient absorption detection.

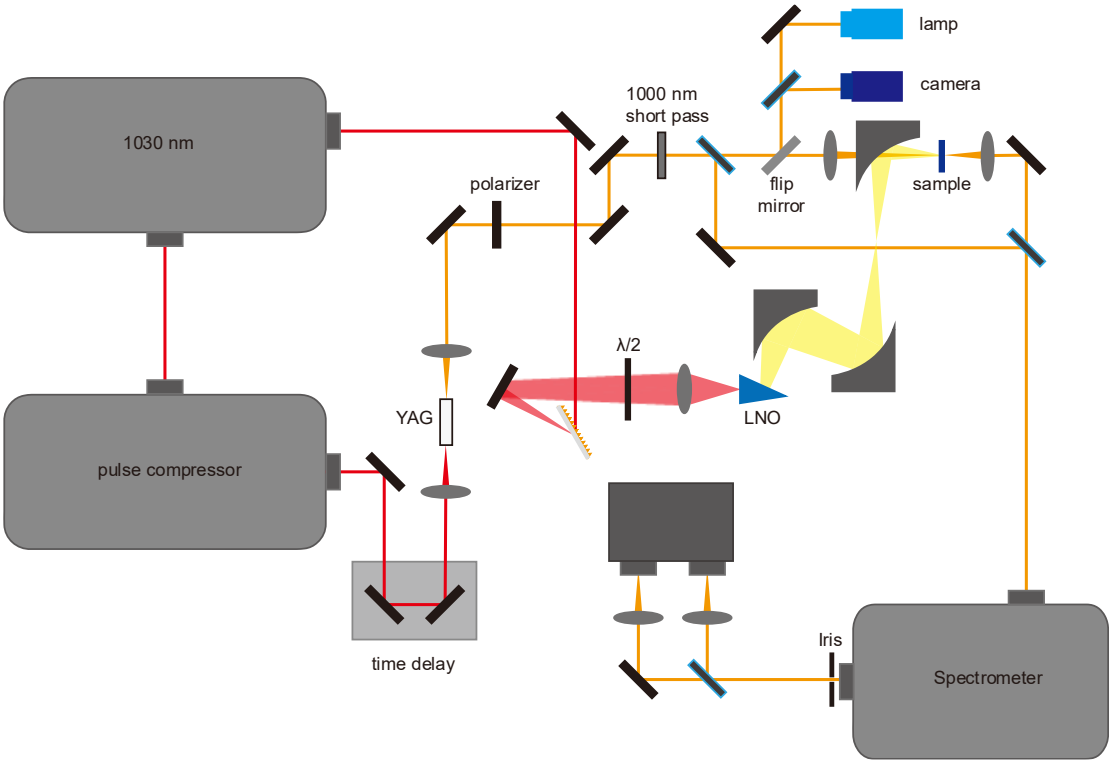

Figure 3.3 Schematic illustration of the home-built THz-pump Transient Absorption setup.

For THz generation, the 1030 nm fundamental beam was directed to a tilted-pulse-front $LiNbO_3$ stage. The beam first passed through a transmission grating, which introduced angular dispersion and thus produced a pulse-front tilt required for phase matching in $LiNbO_3$. After the grating, the beam passed through a half-wave plate and focusing lens before entering the $LiNbO_3$ crystal. The half-wave plate was used to adjust the pump polarization to the appropriate crystallographic direction of the $LiNbO_3$ crystal, while the focusing optics imaged the tilted pulse front into the crystal. Through this so-called optical rectification process, the tilted-pulse-front pump generated a free-space THz pulse. The generated THz beam was then collected, guided, and focused on the sample using a set of off-axis parabolic mirrors.

The white-light probe was generated from the compressed 1030 nm beam. This beam first passed through a mechanical delay stage, which controlled the relative time delay between the THz pump and the optical probe. The mechanical delay stage was placed in the white-light probe arm rather than in the THz pump arm to maintain the stability

of the THz beam path. The THz beam alignment is highly sensitive to small changes in propagation direction or optical path, which can affect the THz focusing point, spatial overlap, and field strength at the sample. In contrast, the white-light probe beam is easier to relay and less sensitive to small path-length changes. Therefore, scanning the probe delay provides a more stable way to control the pump-probe timing without perturbing the THz excitation field.

The delayed 1030 nm pulse was then focused into a YAG crystal to generate broadband white-light probe pulses. After the YAG crystal, the divergent white-light beam was collected and collimated by a lens. The white-light probe then passed through a polarizer to purify the probe polarization and through a 1000 nm short-pass filter to remove the residual 1030 nm fundamental light.

Figure 3.4 shows a schematic illustration of THz EO sampling using GaP crystal with the same white light probe. In this measurement, the THz pulse and probe pulse were spatially and temporally overlapped in the GaP crystal. The THz-induced birefringence changed the polarization state of the probe pulse through the Pockels effect, and this polarization change was converted into a balanced detection signal through a quarter-wave plate, a Wollaston prism, and a balanced photodetector. By scanning the delay between the THz pulse and the probe pulse, a time-domain THz waveform $E_{\mathrm{THz}}(t)$ was obtained. This waveform was used to identify the THz time zero and to verify the THz field profile before performing THz-pump transient absorption measurements.

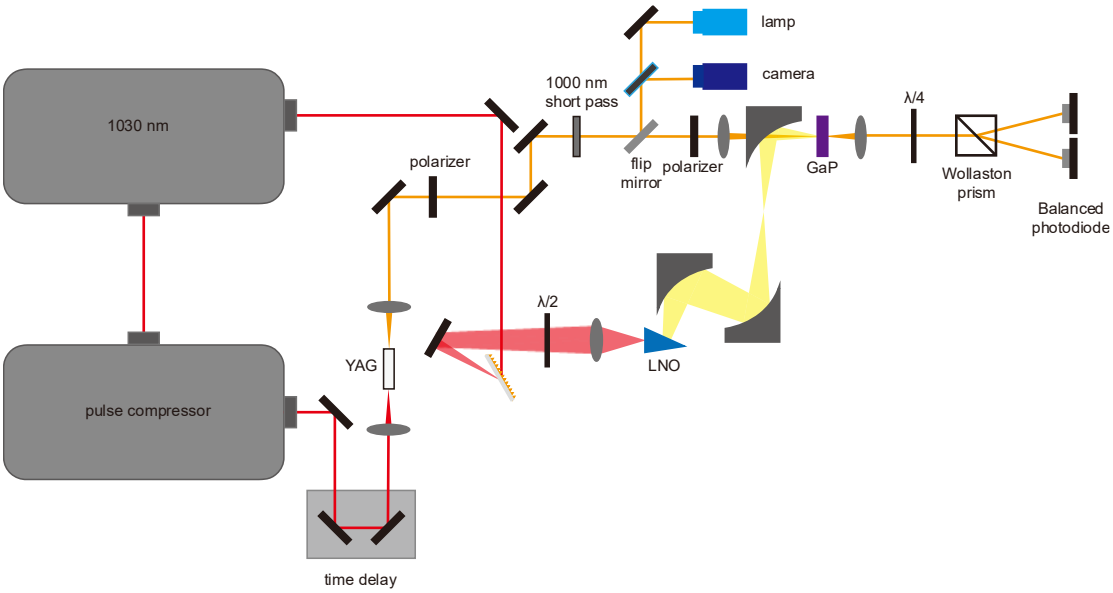

Figure 3.4 Schematic illustration of the home-built GaP-based EO sampling setup.

For transient absorption, in order to increase signal-to-noise ratio, before reaching the sample, the white-light probe was divided into two beams by a beam splitter. One beam served as the reference beam and was directed to the spectrometer without passing through the sample. The other beam served as the sample probe beam. Both beams were sent into the spectrometer and undergo the same spectral selection and finally hit a balanced detector to subtract optics-related noise such as pulse-to-pulse fluctuations and spectral giggling.

A lamp illumination path and a camera imaging path were incorporated to monitor the details of sample surface and beam spatial overlap. Specifically, these imaging components were used to locate the sample region and optimize the focus before data acquisition. During alignment, the camera image was used to adjust the sample position and ensure that the optical probe was focused on the desired area of the film.

The transient absorption signal is defined as the pump-induced change in optical density, which is thereby calculated by:

$$\Delta \mathrm{OD}(\lambda, \mathrm{t}) = \mathrm{OD}_{\mathrm{pumped}}(\lambda, \mathrm{t}) - \mathrm{OD}_{\mathrm{unpumped}}(\lambda, \mathrm{t}) = -\lg \frac{\mathrm{I}_{\mathrm{sample-pump}}}{\mathrm{I}_{\mathrm{sample-unpump}}},$$

In actual experiments, however, we use a lock-in amplifier (SR830, Stanford Research Systems) to directly extract the change of optical intensity:

$$\Delta I = \mathrm{I}_{\mathrm{sample-pump}} - \mathrm{I}_{\mathrm{sample-unpump}}.$$

This is enabled by using the internal Acousto-Optic Modulator to tune the repetition rate of THz pump (12.5 kHz) to be synchronously half of the repetition rate of white light probe (25 kHz). Thus, by locking the 12.5 kHz signal captured by the balanced detector, we can get a high signal-to-noise value of $\Delta \mathrm{I}$. Then through some simple mathematical treatments, we can retrieve the transient absorption signal defined above.

Chapter 4 Results and discussion

This chapter presents the structural, static optical, and THz-induced transient optical properties of CuPc thin films. X-ray diffraction is first used to characterize the film structure and possible polymorphs. The static optical response is then examined by UV-VIS absorption, polarization-dependent absorption, and Raman spectroscopy, which provide information on the Q-band features, optical anisotropy, and vibrational fingerprints.

Based on these characterizations, the final section focuses on the THz-induced transient blue shift observed in the Q-band absorption region. Transient signals measured at different probe wavelengths are compared to identifying the spectral signature of the response and its evolution with pump-probe delay time. In particular, the discussion examines whether the blue shift can be interpreted as a field-induced Stark response driven by the intense THz electric field, and how this transient effect is related to the static optical properties and molecular packing of the CuPc films.

4.1 Structural Characterization

Before discussing the optical response of the CuPc thin films, their structural properties were first examined. The molecular packing and crystalline phase of CuPc can affect intermolecular interactions, optical anisotropy, and the Q-band absorption features. Therefore, X-ray diffraction measurements were performed to characterize the film structure and to provide structural context for the optical measurements discussed in the following sections.

4.1.1 X-ray Diffraction Characterization

Figure 4.1 and Figure 4.2 shows that the XRD patterns of the CuPc films prepared with and without heating are nearly identical, with both films exhibiting a main diffraction peak near $2\theta \approx 18.4°$. The unheated film exhibits a peak at $2\theta = 18.441°$, while the heated film shows a slightly shifted peak at $2\theta = 18.361°$. Based on Bragg's law and assuming Cu Kα radiation, these peaks correspond to d-spacings of approximately 4.80 Å and 4.83 Å, respectively.

To identify the crystalline phase of the toluene-prepared CuPc film, the measured XRD pattern was compared with the XRD pattern of β-form CuPc[26] discussed in Chapter 2. The calculated d-spacings are close to the reported b-axis periodicity of β-form CuPc, approximately 4.79 Å, which is associated with the Cu-Cu repeat distance along the molecular stacking direction.

The small shift of the diffraction peak after heating indicates a slight increase in the calculated spacing. This difference may arise from minor variations in molecular packing, residual strain, film thickness, or experimental uncertainty. However, because the overall XRD patterns remain nearly unchanged and no obvious additional diffraction peaks appear, the heating process does not seem to induce a significant phase transformation. Instead, both films remain consistent with predominantly β-form CuPc.

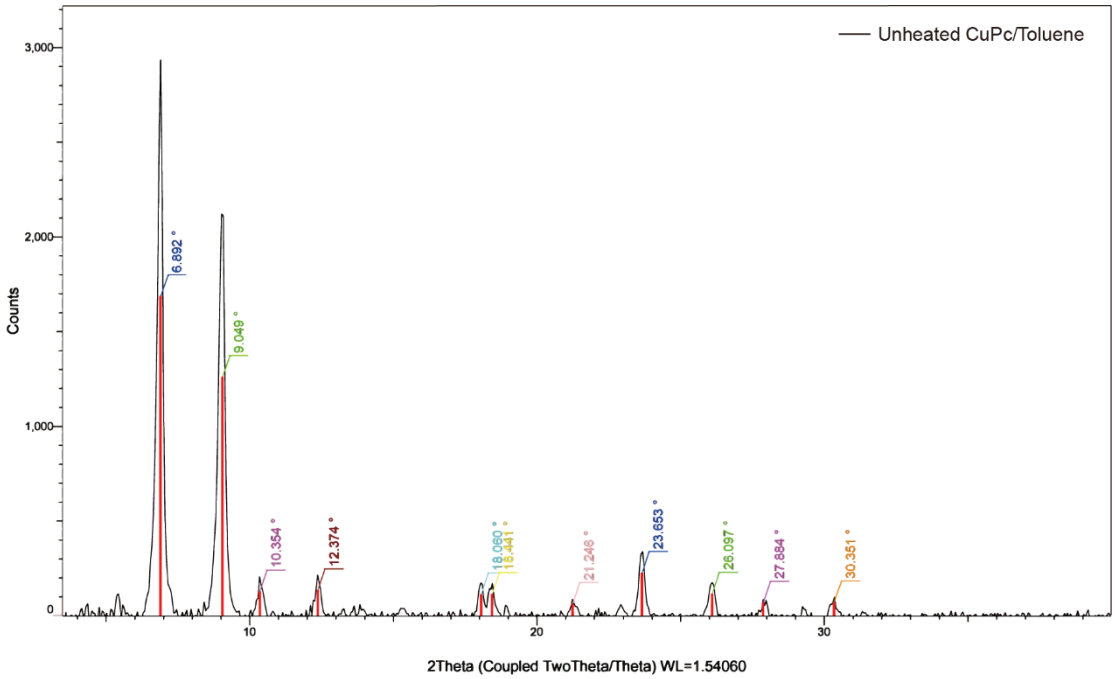

Figure 4.1 XRD pattern of the unheated toluene-prepared CuPc film.

DB Compound Name	Angle	*d* Value	Rel. Intensity
Peak 1	6.88°	12.82 Å	100.0%
Peak 2	9.05°	9.76 Å	74.8%
Peak 3	10.35°	8.54 Å	7.6%
Peak 4	12.37°	7.15 Å	8.0%
Peak 5	18.06°	4.91 Å	6.7%
Peak 6	18.44°	4.81 Å	6.8%
Peak 7	21.25°	4.18 Å	3.7%
Peak 8	23.65°	3.76 Å	13.4%
Peak 9	26.10°	3.41 Å	6.9%
Peak 10	27.88°	3.20 Å	4.2%
Peak 11	30.35°	2.94 Å	4.2%

Table 4.1 XRD peak positions, d-spacings, and relative intensities of the unheated toluene-prepared CuPc film.

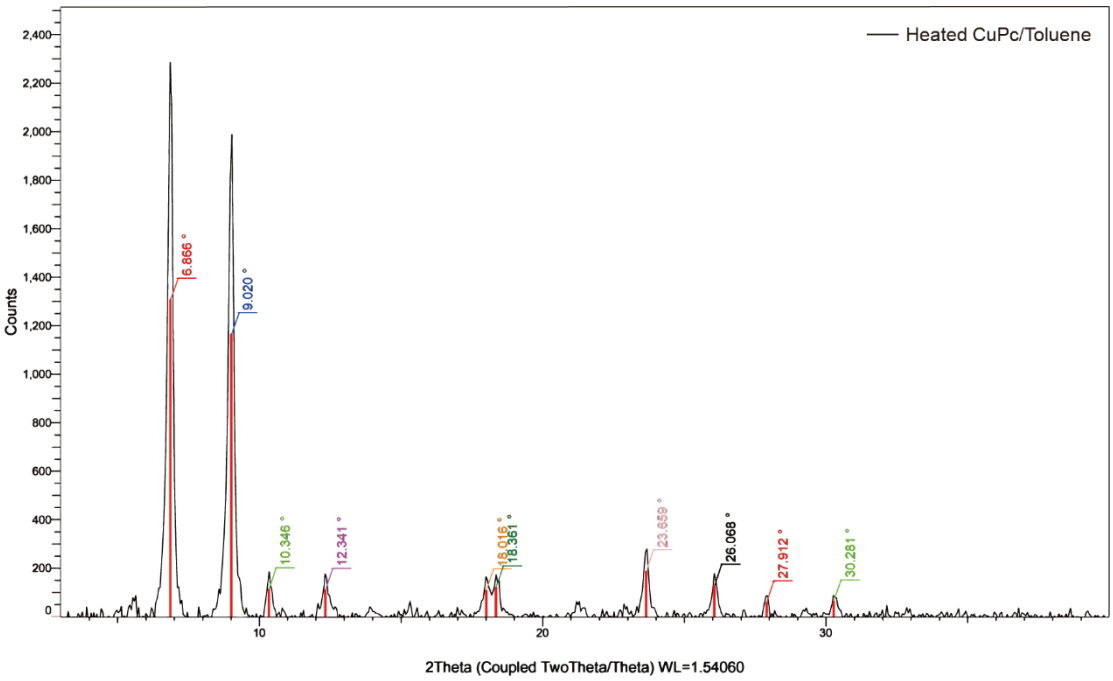

Figure 4.2 XRD pattern of the heated toluene-prepared CuPc film.

DB Compound Name	Angle	*d* Value	Rel. Intensity
Peak 1	6.87°	12.86 Å	100.0%
Peak 2	9.02°	9.80 Å	89.2%
Peak 3	10.35°	8.54 Å	8.7%
Peak 4	12.34°	7.17 Å	8.5%
Peak 5	18.02°	4.92 Å	8.3%
Peak 6	18.36°	4.83 Å	9.3%
Peak 7	23.66°	3.76 Å	14.4%
Peak 8	26.07°	3.42 Å	9.8%
Peak 9	27.91°	3.19 Å	4.6%
Peak 10	30.28°	2.95 Å	4.9%

Table 4.2 XRD peak positions, d-spacings, and relative intensities of the heated toluene-prepared CuPc film.

In contrast, as shown in Figure 4.3, the CuPc film prepared with TFA shows weaker diffraction peaks within the measured range, suggesting the absence of claer long-range crystalline order. And the heated TFA-prepared film in Figure 4.4 shows an even more featureless XRD pattern than the unheated one, suggesting that heating further disrupts the long-range crystalline order rather than promoting crystallization. This comparison indicates that the toluene-prepared film forms a well-defined β-form crystalline structure, whereas the TFA-prepared film is largely amorphous or poorly crystalline.

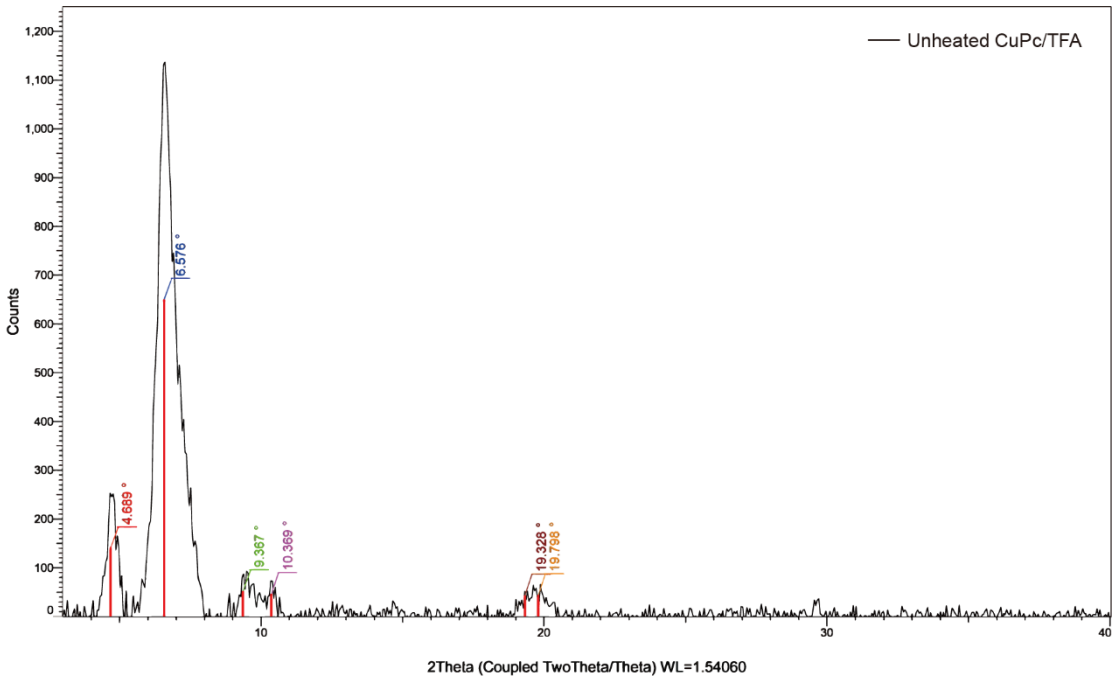

Figure 4.3 XRD pattern of the unheated TFA-prepared CuPc film.

DB Compound Name	Angle	*d* Value	Rel. Intensity
Peak 1	4.69°	18.83 Å	21.5%
Peak 2	6.58°	13.43 Å	100.0%
Peak 3	9.37°	9.43 Å	8.0%
Peak 4	10.37°	8.52 Å	7.1%
Peak 5	19.33°	4.59 Å	6.6%
Peak 6	19.80°	4.48 Å	6.8%

Table 4.3 XRD peak positions, d-spacings, and relative intensities of the unheated TFA-prepared CuPc film.

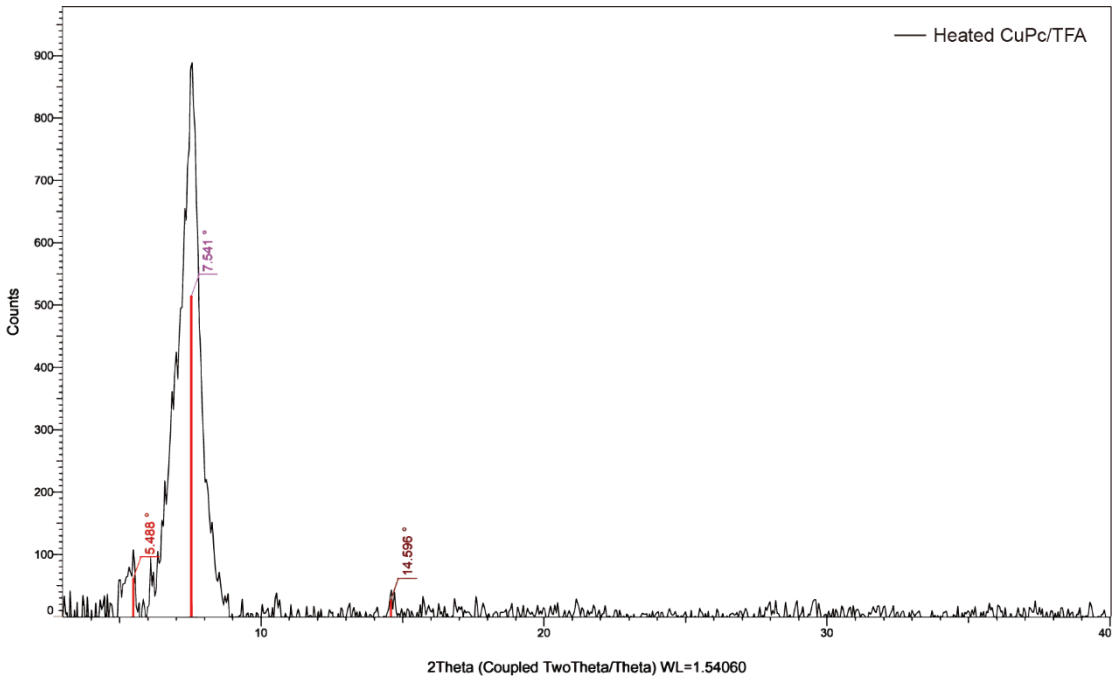

Figure 4.4 XRD pattern of the heated TFA-prepared CuPc film.

DB Compound Name	Angle	*d* Value	Rel. Intensity
Peak 1	5.49°	16.09 Å	12.0%
Peak 2	7.54°	11.71 Å	100.0%
Peak 3	14.596°	6.06 Å	5.3%

Table 4.4 XRD peak positions, d-spacings, and relative intensities of the heated TFA-prepared CuPc film.

Therefore, based on the consistency between the measured XRD peak, the calculated d-spacing, and the literature β-CuPc reference pattern, the toluene-prepared CuPc film is assigned to the β-form.

4.2 Static Optical properties

After the structural characterization, the static optical properties of the CuPc films were examined to establish the spectral baseline for the transient optical measurements. UV-VIS absorption spectroscopy was first used to characterize the electronic absorption features, especially the Q-band region where the THz-induced transient blue shift is observed. Polarization-dependent absorption measurements were then performed to investigate the optical anisotropy of films, which is related to molecular orientation and packing. These static optical measurements provide

essential reference information for interpreting the wavelength-dependent transient response discussed in the following section.

4.2.1 UV-VIS Spectroscopy

UV-VIS absorption spectroscopy was performed to examine the electronic absorption features of the TiOPc/TFA, H_2Pc/toluene, CuPc/TFA, CuPc/toluene films and CuPc/TFA solution. The focus is the Q-band region, where H_2Pc, CuPc and TiOPc exhibits strong visible absorption associated with π-π^* transitions of the macrocycle.

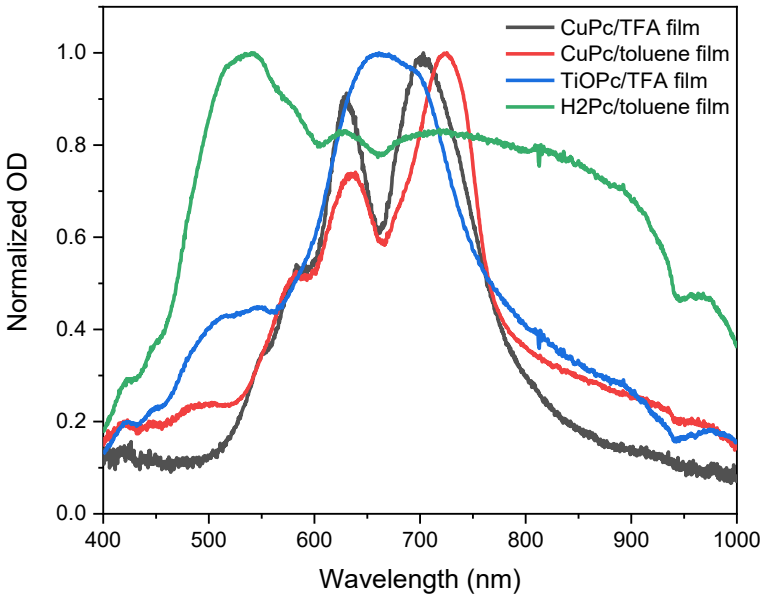

Figure 4.5 Normalized UV-VIS absorption spectra of TiOPc/TFA, H_2Pc/toluene, CuPc/TFA, and CuPc/toluene films.

Figure 4.5 shows the normalized UV-VIS absorption spectra of different phthalocyanine films in the wavelength range of 400-1000 nm. The CuPc/TFA and CuPc/toluene films show two clear absorption peaks between approximately 590 and 770 nm. For the CuPc/TFA film, the two peaks are located near 630 and 700 nm. In comparison, the lower-wavelength peak of the CuPc/toluene film remains near 630 nm, while the higher-wavelength peak is slightly red-shifted to around 725 nm. By comparison with the CuPc reference spectrum shown in Figure 2.3, these two peaks can be assigned to the Q-band absorption of CuPc. The shift of the higher-wavelength Q-band peak may be related to differences in molecular aggregation, packing environment, or film morphology caused by different film preparation conditions.

In contrast, the TiOPc/TFA film exhibits a much broader and stronger absorption feature centered near 660 nm, rather than two well-resolved Q-band peaks. This broadening may arise from the lower molecular symmetry, the nonplanar structure associated with the axial Ti=O group, and stronger aggregation or disorder effects in the film. The H_2Pc/toluene film also shows a broad absorption band over the 600-800 nm region, rather than two sharp and well-separated peaks. These differences indicate that the central metal ion and molecular symmetry strongly affect the Q-band absorption features of phthalocyanine films.

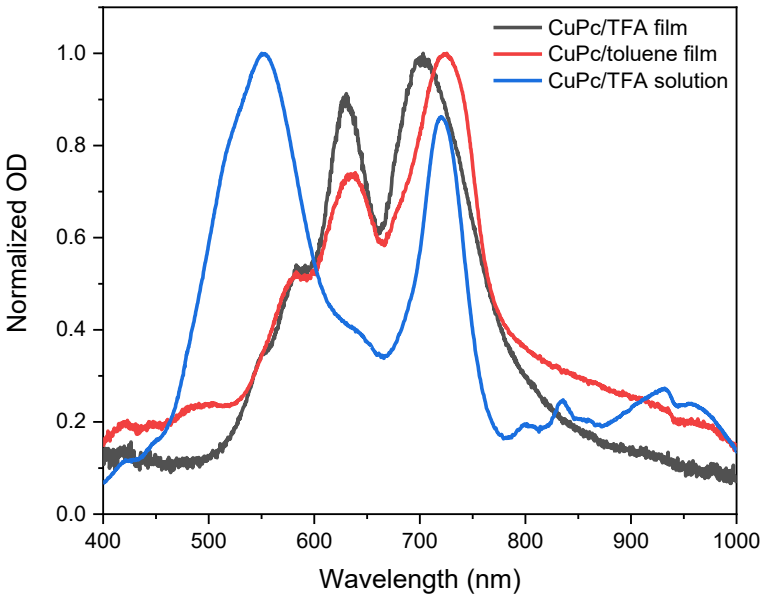

Figure 4.6 Normalized UV-VIS absorption spectra of CuPc/TFA, CuPc/toluene films and CuPc/TFA solution.

The normalized UV-VIS absorption spectra in Figure 4.6 compare CuPc/TFA and CuPc/toluene films with the CuPc/TFA solution over the wavelength range of 400-1000 nm. The CuPc/TFA solution represents one clear peak at 720 nm, while both CuPc films exhibit two resolved absorption features in the Q-band region. Compared with the Q-band of CuPc solution in Figure 2.3, where the peak is around 680 nm, the Q-band peak of the CuPc/TFA solution has obvious red shift. Previous studies have shown that CuPc can form protonation forms in solutions containing TFA, with uneven protonation leading to a redshift in Q-band characteristics and molecular symmetry decreasing. Therefore, the observed red shifted Q-band in CuPc/TFA solution may be related to TFA induced protonation.

The appearance of two Q-band peaks in the films indicates stronger intermolecular coupling in the solid state, which is related to the molecular aggregation and π-stacking of CuPc molecules. In CuPc thin films, this Q-band splitting has been commonly attributed to Davydov splitting caused by the interaction between adjacent molecules in the crystal or aggregated phase. In particular, Figure 2.3 shows predominant Q-band peaks near 640 and 725 nm in β-CuPc thin films, which are very similar to the peak positions and overall lineshape observed for the CuPc/toluene film in this work. This similarity further supports the assignment of the CuPc/toluene film to the β-form structure, consistent with the XRD results discussed above. But the CuPc/TFA film shows a less clear β-form spectral signature, possibly due to residual protonation, disorder, or acid induced molecular stacking disruption during film formation, which prevents CuPc/TPA films from forming a clear β-form stacking.

Overall, the UV-VIS results suggest that the CuPc/toluene film has a clear Q-band structure associated with intermolecular coupling and molecular stacking. This makes the CuPc/toluene film a suitable system for the following THz-pump optical-probe measurements, where a clear static absorption spectrum is important for identifying transient spectral shifts. And to further confirm the molecular orientation and optical anisotropy of this system, we did the absorption anisotropy measurements in next section.

4.2.2 Absorption Anisotropy

In the absorption anisotropy measurement for both CuPc/toluene film and CuPc/TFA film, three different regions were selected for comparison: two small-aperture regions and one large-aperture region (Figure 4.7 B and C). The two small-aperture regions have a diameter of approximately 40 μm and correspond to a lighter-colored area and a darker-colored area, respectively. And the darker region is associated with stronger molecular aggregation. The large-aperture region, with a diameter of approximately 2 cm, includes both darker and lighter areas and therefore represents a spatially averaged response over a larger film area.

The polarization-dependent absorption polar plots in Figure 4.7 generally exhibit a dumbbell-like shape, indicating a uniaxial-like absorption anisotropy. This behavior is consistent with the expected anisotropic optical response of CuPc films, where ordered molecular packing or π-stacked domains can make the absorption stronger along one preferred direction.

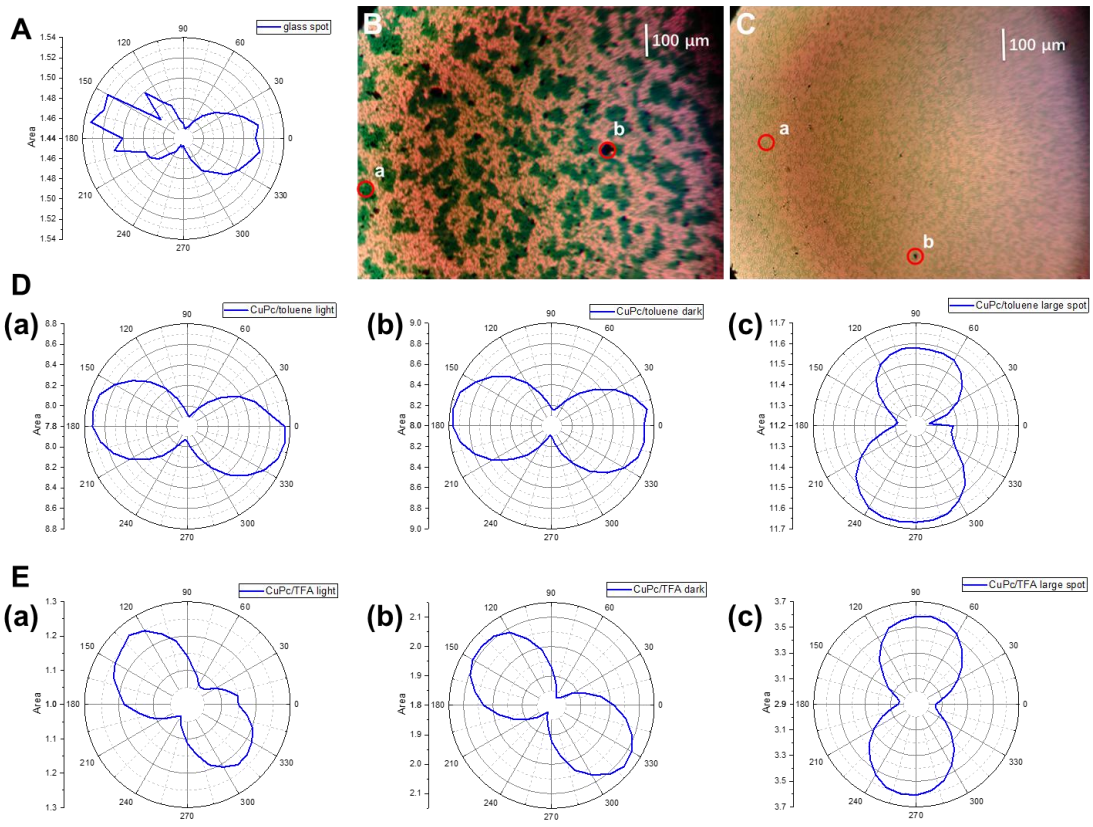

Figure 4.7 Absorption anisotropy measurements of CuPc/toluene and CuPc/TFA films. (A) Polar plot of the polarization-dependent absorbance from the glass substrate. (B) and (C) Optical microscopy images of the CuPc/toluene and CuPc/TFA films, respectively. The red circles mark the light-colored region (a) and dark-colored region (b) selected for small-aperture measurements. (D) Polar plots of the CuPc/toluene film measured from: (a) light-colored small-aperture region, (b) dark-colored small-aperture region, and (c) large-aperture region. (E) Polar plots of the CuPc/TFA film measured from: (a) light-colored small-aperture region, (b) dark colored small-aperture region, and (c) large-aperture region.

For the CuPc/toluene film, the anisotropy factors are 0.0352 for the light-colored small-aperture region, 0.0351 for the dark-colored small-aperture region, and 0.0119 for the large-aperture region (Figure 4.7 D). These values indicate that the CuPc/toluene film exhibits weak but measurable local absorption anisotropy. The nearly identical anisotropy factors obtained from the light and dark small-aperture regions suggest that the local polarization anisotropy is not strongly affected by the local absorption intensity or aggregation density. In contrast, the anisotropy factor decreases significantly for the large-aperture measurement, indicating that the film becomes more optically isotropic when averaged over a larger area.

This behavior can be understood in terms of spatial averaging over molecular domains. In a small probing area, the measurement samples a limited number of molecular aggregates or domains. Within such a local region, CuPc molecules may exhibit a preferential orientation associated with π-stacking or ordered molecular packing, leading to a weak polarization-dependent absorption response. In the large-aperture measurement, however, many domains with different in-plane orientations are sampled simultaneously. The anisotropic responses from these differently oriented domains are averaged out, resulting in a much smaller anisotropy factor. Therefore, the CuPc/toluene film can be described as locally anisotropic but macroscopically nearly isotropic.

But for CuPc/TFA film, which is shown in Figure 4.7 E, it exhibits a noticeably different polarization response. The anisotropy factors obtained from the light-colored small-aperture region, dark-colored small-aperture region, and large-aperture region are 0.0673, 0.0512, and 0.0630, respectively. Unlike the CuPc/toluene film, where the anisotropy factor decreases significantly from the small-aperture to the large-aperture measurement, the CuPc/TFA film shows comparable anisotropy factors for all three regions. This indicates that the polarization-dependent absorption in the CuPc/TFA film does not strongly depend on the probing area or the local aggregation contrast.

A possible explanation is the chemical modification of CuPc by TFA. TFA can protonate the meso-bridging aza-nitrogen sites of the CuPc macrocycle. Depending on the degree of protonation, a distribution of protonated CuPc species, including mono-, di-, tri-, and possibly tetra-protonated CuPc, may be formed. Previous studies have shown that protonation of CuPc can induce Q-band red shifts and splitting, which are associated with reduced molecular symmetry and disrupted intermolecular stacking. Therefore, the polarization-dependent absorption in the CuPc/TFA film may be governed less by well-defined β-form π-stacking and more by protonation-induced changes in the molecular structure and packing environment.

Therefore, the anisotropy results suggest that the CuPc/toluene film contains locally ordered π-stacked domains whose anisotropy is averaged out over a larger area. But the CuPc/TFA film shows a more spatially persistent anisotropic response likely related to TFA-induced protonation and acid-modified molecular packing. More importantly, the anisotropy analysis was performed around the higher-wavelength Q-band feature, which is also the spectral region where the pronounced THz-induced transient blue shift is observed in Section 4.3.

4.2.3 Low-wavenumber Raman

Low-wavenumber Raman spectroscopy was performed on TiOPc, H_2Pc, and CuPc films prepared from toluene in the range of 10-440 cm^{-1}. This spectral region includes both very low-frequency lattice or external modes and low-energy intramolecular deformation modes. The Raman features below approximately 50 cm^{-1} are broadly assigned to lattice-related vibrations, such as intermolecular translations, librations, or collective motions of molecular aggregates, which can be sensitive to molecular packing and intermolecular interactions. Therefore, these low-frequency peaks can provide information about the solid-state packing environment of the phthalocyanine films.

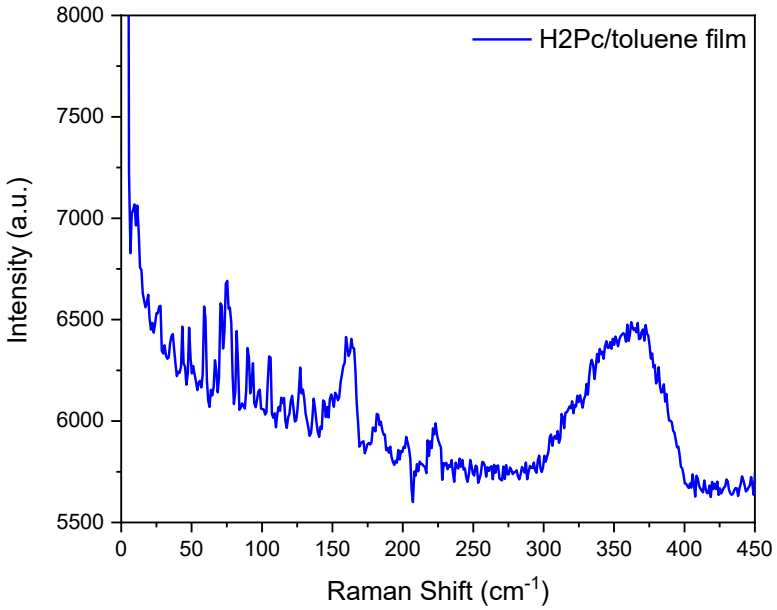

Figure 4.8 Low-wavenumber Raman spectrum of the H_2Pc/toluene film.

In Figure 4.8, H_2Pc only shows multiple weak low-wavenumber features near 9.5, 11.4, 27.0, 43.4, and 48.2 cm^{-1}, their intensities are close to the noise level and the spectrum does not show clearly resolved low-frequency modes. This weak and poorly defined response may be related to weaker ordering, stronger structural disorder, or a less favorable Raman response under the present measurement conditions.

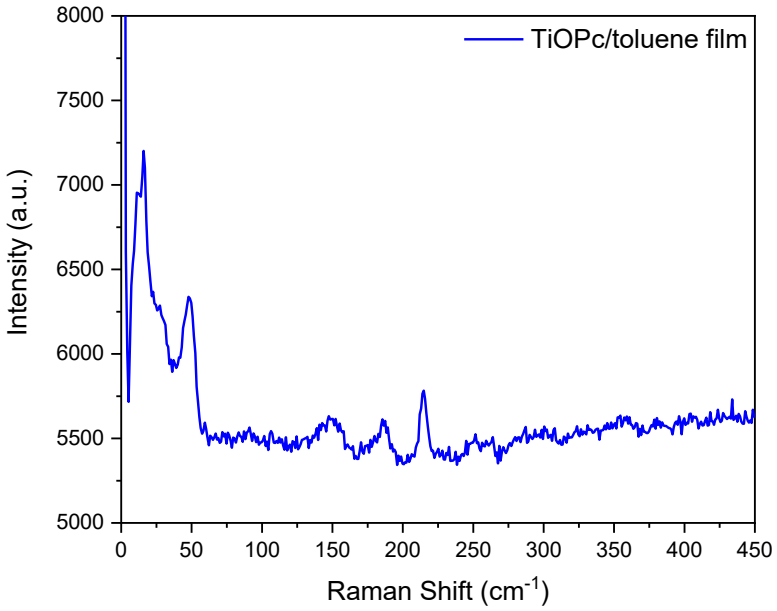

Figure 4.9 Low-wavenumber Raman spectrum of the TiOPc/toluene film.

But more distinct low-wavenumber Raman peaks are shown in the TiOPc/toluene film. The strongest feature appears near 15.9 cm^{-1}, followed by a peak near 11.1 cm^{-1}, and a weaker feature near 47.8 cm^{-1}. The appearance of these peaks indicates that TiOPc possesses measurable low-energy vibrational modes in this spectral region. These modes are likely associated with low-frequency lattice or external vibrations, which are sensitive to molecular packing and intermolecular interactions in the film. In addition, the nonplanar molecular structure of TiOPc, caused by the axial Ti=O group, may influence its low-frequency vibrational response by modifying the molecular symmetry, packing environment, and Raman selection rules.

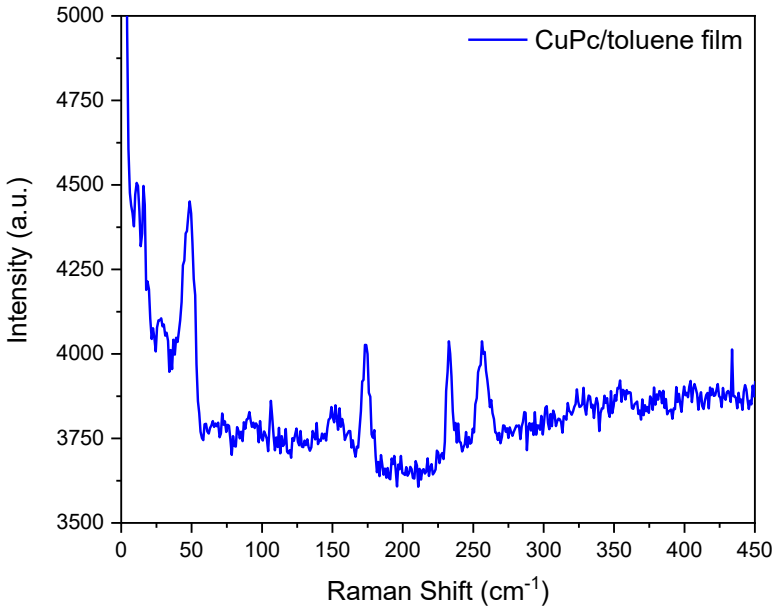

Figure 4.10 Low-wavenumber Raman spectrum of the CuPc/toluene film.

Compared with H_2Pc and TiOPc, the CuPc/toluene film shows a more clearly resolved low-wavenumber Raman response. In particular, the peaks near 11.0, 15.8, and 48.6 cm^{-1} have comparable intensities, indicating that CuPc has multiple well-defined low-energy vibrational modes. In particular, the pronounced CuPc mode near 48.6 cm^{-1}, corresponding to approximately 1.46 THz. Therefore, the CuPc/toluene film may contain clear low-energy vibrational modes in the same frequency range as the THz excitation.

However, this feature should not be directly assigned to a pure out-of-plane vibration of the central Cu ion in an ideal isolated CuPc molecule. CuPc is a planar molecule with approximate D_{4h} symmetry and an inversion center. Under this symmetry, the central-metal out-of-plane vibration is expected to have ungerade symmetry and is therefore infrared active but Raman inactive according to the mutual exclusion rule. Therefore, the Raman feature near 48.6 cm^{-1} is more safely assigned to a low-frequency lattice or external mode, a collective motion of molecular aggregates, or a weakly activated mode caused by symmetry breaking in the solid film.

Although a Raman-active mode is not necessarily directly driven by the THz electric field, the presence of well-defined vibrational features in the THz frequency range suggests that THz excitation may couple to, perturb, or indirectly interact with low-energy molecular or lattice motions in the film. Compared with H_2Pc and TiOPc,

CuPc may therefore be the most suitable system for the subsequent THz-induced transient optical study because it combines well-resolved Q-band absorption, β-form-like packing, and clear low-frequency Raman features in the THz range.

4.3 THz-induced Transient Blue Shift

Figure 4.11 shown below presents the THz-pump transient absorption response of the CuPc/toluene film measured in the visible spectral range from 580 to 700 nm. The two-dimensional false-color map shows the pump-induced optical density change, ΔOD, as a function of probe wavelength and pump-probe time delay. A spectral line cut extracted at time-zero as well as a temporal line cut extracted at 700 nm are also shown. In addition, the corresponding waveform of pump THz electric-field and its Fourier-transform spectrum are shown on Figure 4.12. Together, these measurements allow the transient optical response to be directly compared with the temporal profile and frequency content of the driving THz pulse.

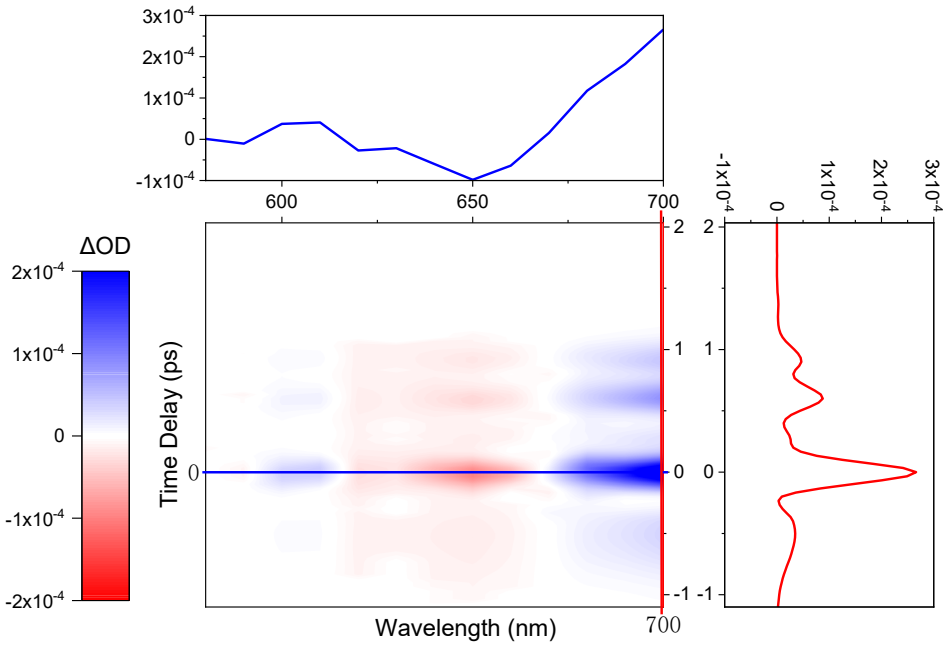

Figure 4.11 THz-induced transient absorption response of the CuPc/toluene film from 580 to 700 nm.

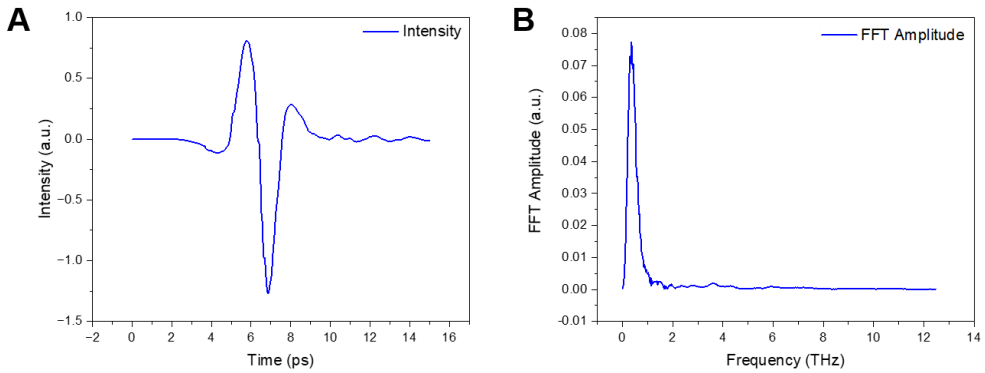

Figure 4.12 Time- and frequency-domain characterization of the THz pulse. (A) Time-domain THz electric-field waveform. (B) Corresponding Fourier-transform amplitude spectrum.

As the transient absorption signal shown in section 3.5, the positive ΔOD indicates an increase in optical density after THz excitation, while negative ΔOD indicates a decrease in optical density. In the color map, the signal amplitude is on the order of 10^{-4}, indicating that the THz-induced optical response is relatively weak but clearly resolved above the background level. The response is concentrated near time zero and decays rapidly within approximately one to two picoseconds, showing that the observed signal is directly associated with the impulsive THz excitation rather than a long-lived thermal or population effect.

Another important feature is that the THz electric field is bipolar, containing both positive and negative field cycles, whereas the measured transient optical response does not reverse sign with the field polarity. This behavior suggests that the signal is unlikely to arise from a response that is linear in the THz electric field, such as a purely first-order Stark effect. Instead, the response is more consistent with an even-order, quadratic-field-dependent process. This even-order response may include a conventional quadratic Stark contribution, which depends on the square of the electric field, but it may also involve field-induced modification of the excitonic state, such as enhanced charge-transfer character and reduced exciton binding energy. Therefore, the comparison between the transient optical signal and the THz waveform suggests that the observed response is not dominated by a linear Stark effect, but is more likely associated with an even-order Stark-like or field-induced excitonic process.

The most pronounced transient feature appears in the long-wavelength region of the measured spectral window, especially near 680-700 nm. Around time zero, this region shows a strong positive ΔOD signal. At the same time, two weaker responses are

observed to be negative around 640-660 nm and positive around 590-620 nm. If comparing with the static absorption spectra of the same sample, this positive-negative-positive spectral pattern clearly resembles two derivative-like lineshapes, which indicate a THz-induced blueshift for both Q-bands for CuPc. Additionally, the blueshift of lower energy Q-band is much larger than the other.

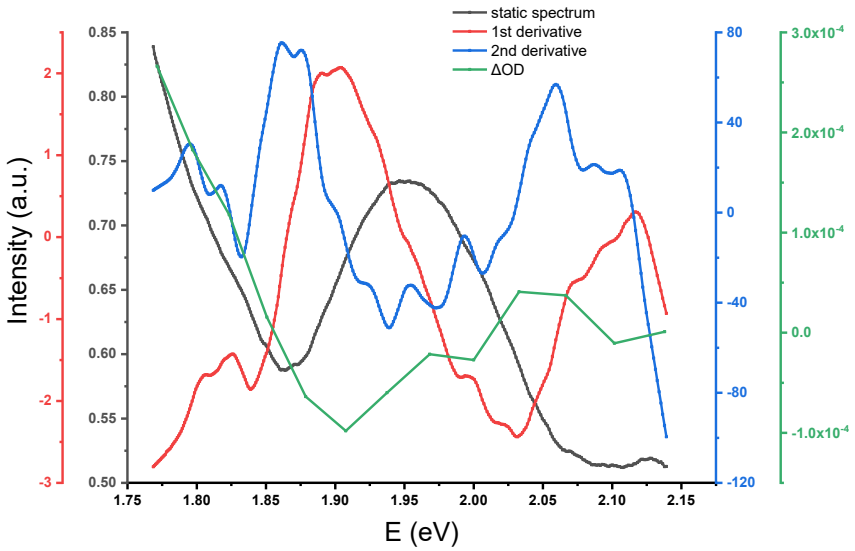

Figure 4.13 Comparison of transient ΔOD with derivative spectra of the static absorption.

To identify the dominant spectral origin of the transient response, the measured ΔOD spectrum was compared with the first and second derivatives of the static absorption spectrum with respect to photon energy in Figure 4.13. The transient ΔOD shows a much stronger resemblance to the first-derivative lineshape than to the second-derivative lineshape. More specifically, as shown in Figure 4.14 below, when the negative first derivative of the static absorption spectrum is plotted, its spectral shape agrees well with the measured ΔOD. Since a small shift of the absorption band gives

$$\Delta OD(E) \approx -\delta E \frac{dOD_0(E)}{dE},$$

the negative first-derivative-like response indicates that the THz field primarily induces a shift of the absorption feature toward higher photon energy, namely a transient blueshift. Table 4.5 also shown that the negative first-derivative model provides a significantly better fit than the second-derivative model, indicating that the transient response is dominated by a blue-shift-like spectral shift rather than field-induced broadening.

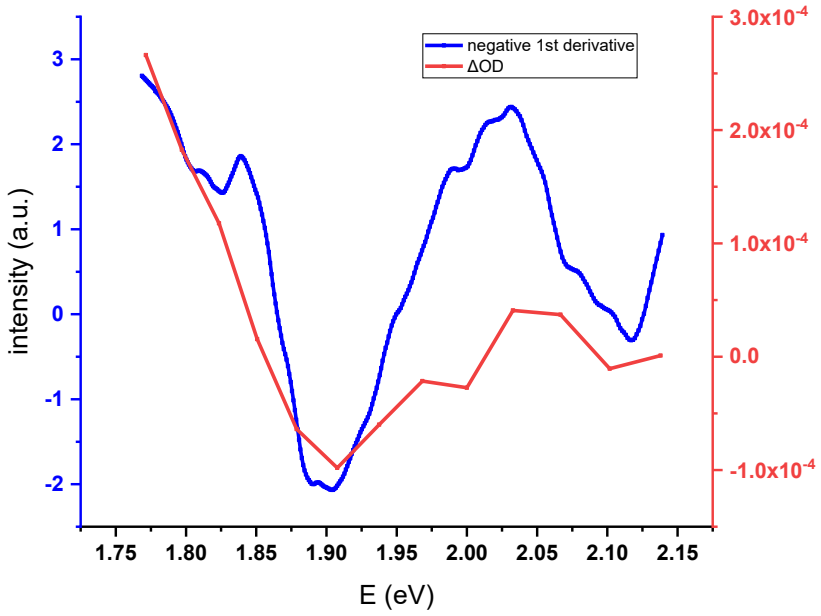

Figure 4.14 Comparison of transient ΔOD with negative 1st derivative spectra of the static absorption.

Fitting model	R^2	Adjusted R^2	Residual sum of squares	p-value
Negative first derivative	0.59846	0.56196	5.17×10^{-8}	0.00192
Second derivative	0.04696	-0.03968	1.23×10^{-7}	0.47699

Table 4.5 Derivative lineshape fitting results for the THz-induced transient ΔOD spectrum.

The physical origin of this field-induced blueshift can be understood as a competition between two effects[74]. The first contribution is the conventional Stark shift of the excitonic transition. In the present CuPc system, the response is expected to be dominated by the quadratic Stark effect because the molecular symmetry strongly suppresses the permanent dipole contribution. The quadratic Stark shift can be written as

$$\delta E_{\text{Stark}} = -\frac{1}{2}\Delta\alpha F^2,$$

where $\Delta\alpha=\alpha_e-\alpha_g$ is the difference in polarizability between the excited and ground states. If the excited state is more polarizable than the ground state, $\Delta\alpha>0$, this term lowers the transition energy and therefore produces a redshift.

The second contribution is the field-induced modification of the exciton binding energy. The optical exciton energy can be approximately described as

$$E_{\text{exciton}} = E_{\text{gap}} - E_b,$$

where E_b is the electron-hole Coulomb binding energy[67]. Under an external electric field, especially for excitons with at least partial charge-transfer or delocalized character, the electron and hole can be spatially separated more efficiently. This field-driven charge separation reduces the effective Coulomb binding energy. Since smaller E_b increases E_{exciton}, this contribution produces a blueshift.

Therefore, the observed net spectral shift reflects the competence between the conventional quadratic Stark redshift and the binding-energy-reduction-induced blueshift. For CuPc films, the molecular stacking structure provides an efficient pathway for intermolecular charge-transfer. Since Q-band exciton is not purely Frenkel-like but contains Frenkel-CT mixed character, we therefore propose that the applied THz electric field enhances the CT character by driving electron-hole separation along the stacked molecular structure, leading to a substantial reduction of the effective exciton binding energy. In this case, the blueshift associated with binding energy reduction can overcome the conventional quadratic Stark redshift, resulting in an observed net transient blueshift of the Q-band absorption.

Chapter 5 Conclusion

In this work, the THz-induced transient optical response of CuPc thin films was investigated with particular focus on the Q-band absorption region. By comparing the measured transient ΔOD spectrum with the first and second derivatives of the static absorption spectrum, the transient signal are closer to the negative first derivative of the static absorption spectrum, indicating that the dominant spectral response is a transient shift of the Q-band absorption toward higher photon energy, namely a field-induced blueshift.

This observation is notable because the conventional quadratic Stark effect is generally expected to produce a redshift when the excited state has a larger polarizability than the ground state. In such a picture, the external electric field stabilizes the more polarizable excited state more strongly, thereby lowering the transition energy. However, the exciton transition energy is also determined by the Coulomb binding energy between the electron and hole. For excitons with delocalized or partial charge-transfer character, an applied electric field can separate the electron and hole more effectively, reducing the effective exciton binding energy. Since the exciton energy can be described approximately as the band-gap energy minus the exciton binding energy, a reduction in binding energy increases the exciton transition energy and therefore gives rise to a blueshift.

We therefore interpret the observed Q-band blueshift as a competition between the conventional quadratic Stark redshift and a binding-energy-reduction-induced blueshift. In CuPc thin films, the Q-band exciton is expected to have mixed Frenkel and charge-transfer character. The stacked molecular structure may provide an efficient pathway for field-driven intermolecular charge separation. Under the applied THz electric field, the CT contribution can be enhanced, reducing the effective exciton binding energy. When this blueshift contribution exceeds the conventional Stark redshift, the net transient response appears as the observed Q-band blueshift.

Future work should focus on improving the structural quality and orientational control of CuPc films. The drop-cast films used in this study may contain morphological disorder, mixed domains, and spatially varying molecular packing. More controlled film preparation methods, such as thermal evaporation, vacuum deposition, or other vapor-phase growth techniques, could produce smoother, more uniform, and more oriented CuPc thin films. Such samples would allow a clearer correlation between

molecular packing, Frenkel-CT mixing, and the magnitude and sign of the THz-induced spectral shift.

Another important future direction is polarization-dependent THz-pump optical-probe spectroscopy. If the field-induced blueshift is closely related to intermolecular stacking and field-driven charge separation, then the response should depend strongly on the direction of the applied THz electric field relative to the preferred stacking direction of the molecules. If the THz field is aligned along the molecular stacking direction, it may drive intermolecular charge separation more efficiently and produce a stronger blueshift. In contrast, a perpendicular field direction may lead to a weaker response. Therefore, polarization-resolved THz-pump optical-probe measurements could directly test whether the blueshift is associated with directional CT-mediated electron–hole separation.

A further important direction is field-strength-dependent measurement. If the observed blueshift originates from field-assisted charge separation, its magnitude may not increase linearly or simply quadratically with THz field strength. Instead, there may be threshold-like behavior. Below a certain field strength, the electric field may be too weak to overcome the intermolecular charge-transfer barrier or the Coulomb attraction between the electron and hole, and little or no blueshift would be observed. Above this threshold, the field could efficiently enhance CT character and spatially separate the electron and hole, leading to a rapid increase of the blueshift amplitude. Measuring the Q-band shift as a function of THz field strength would therefore help distinguish a conventional Stark response from a CT-mediated binding-energy-reduction mechanism.

Overall, these results suggest that the THz-induced response of CuPc thin films cannot be understood solely within the framework of a conventional quadratic Stark redshift. Instead, the transient Q-band blueshift points to the important role of intermolecular electronic coupling, Frenkel-CT mixing, and field-induced modification of exciton binding energy. This interpretation highlights CuPc thin films as a useful platform for studying how ultrafast electric fields can manipulate excitonic states in molecular semiconductors. More controlled film growth and polarization-resolved measurements will be essential for further verifying whether the binding-energy-reduction-induced blueshift can overcome the conventional Stark redshift and produce the net transient blueshift observed in the Q-band absorption.

References

[1] Nitzan, A. and M.A. Ratner, *Electron Transport in Molecular Wire Junctions.* Science, 2003. **300**(5624): p. 1384-1389.
[2] Aviram, A. and M.A. Ratner, *Molecular rectifiers.* Chemical Physics Letters, 1974. **29**(2): p. 277-283.
[3] Tsutsui, M. and M. Taniguchi, *Single Molecule Electronics and Devices.* Sensors, 2012. **12**(6): p. 7259-7298.
[4] Friedman, J.R. and M.P. Sarachik, *Single-molecule nanomagnets.* Annu. Rev. Condens. Matter Phys., 2010. **1**(1): p. 109-128.
[5] Gould, C.A., et al., *Ultrahard magnetism from mixed-valence dilanthanide complexes with metal-metal bonding.* Science, 2022. **375**(6577): p. 198-202.
[6] Ajayan, J., et al., *Ferroelectric Field Effect Transistors (FeFETs): Advancements, challenges and exciting prospects for next generation Non-Volatile Memory (NVM) applications.* Materials Today Communications, 2023. **35**: p. 105591.
[7] Kumar, A., V. Kumar Vashistha, and D. Kumar Das, *Recent development on metal phthalocyanines based materials for energy conversion and storage applications.* Coordination Chemistry Reviews, 2021. **431**: p. 213678.
[8] Lous, R., *Ferroelectric memory devices.* How to store information of the future, 2011.
[9] Kampfrath, T., K. Tanaka, and K.A. Nelson, *Resonant and nonresonant control over matter and light by intense terahertz transients.* Nature Photonics, 2013. **7**(9): p. 680-690.
[10] Leitenstorfer, A., et al., *The 2023 terahertz science and technology roadmap.* Journal of Physics D: Applied Physics, 2023. **56**(22): p. 223001.
[11] Boxer, S.G., *Stark Realities.* The Journal of Physical Chemistry B, 2009. **113**(10): p. 2972-2983.
[12] Lu, X., et al., *Scanning Tunneling Microscopy of Metal Phthalocyanines: d7 and d9 Cases.* Journal of the American Chemical Society, 1996. **118**(30): p. 7197-7202.
[13] Liao, M.-S. and S. Scheiner, *Electronic structure and bonding in metal phthalocyanines, Metal=Fe, Co, Ni, Cu, Zn, Mg.* The Journal of Chemical Physics, 2001. **114**(22): p. 9780-9791.
[14] Nyokong, T., *Effects of substituents on the photochemical and photophysical properties of main group metal phthalocyanines.* Coordination Chemistry Reviews, 2007. **251**(13): p. 1707-1722.
[15] Klofta, T., et al., *Photoelectrochemical and spectroscopic characterization of thin films of titanyl phthalocyanine: comparisons with vanadyl phthalocyanine.* Journal of Physical Chemistry, 1987. **91**(22): p. 5646-5651.
[16] Ziolo, R.F., C.H. Griffiths, and J.M. Troup, *Crystal structure of vanadyl phthalocyanine, phase II.* Journal of the Chemical Society, Dalton Transactions, 1980(11): p. 2300-2302.

[17] Silver, J., et al., *Electrochromism in titanyl and vanadyl phthalocyanine thin films.* Journal of Materials Chemistry, 1991. **1**(5): p. 881-888.
[18] Karan, S. and B. Mallik, *Templating Effects and Optical Characterization of Copper (II) Phthalocyanine Nanocrystallites Thin Film: Nanoparticles, Nanoflowers, Nanocabbages, and Nanoribbons.* The Journal of Physical Chemistry C, 2007. **111**(20): p. 7352-7365.
[19] Gouterman, M., G.H. Wagnière, and L.C. Snyder, *Spectra of porphyrins: Part II. Four orbital model.* Journal of Molecular Spectroscopy, 1963. **11**(1): p. 108-127.
[20] Rosa, A. and E. Baerends, *Metal-macrocycle interaction in phthalocyanines: density functional calculations of ground and excited states.* Inorganic Chemistry, 1994. **33**(3): p. 584-595.
[21] Mack, J. and M.J. Stillman, *Assignment of the Optical Spectra of Metal Phthalocyanine Anions.* Inorganic Chemistry, 1997. **36**(3): p. 413-425.
[22] del Pino Rosendo, E., et al., *Symmetry-breaking charge transfer and intersystem crossing in copper phthalocyanine thin films.* Physical Chemistry Chemical Physics, 2023. **25**(9): p. 6847-6856.
[23] Farag, A., *Optical absorption studies of copper phthalocyanine thin films.* Optics & Laser Technology, 2007. **39**(4): p. 728-732.
[24] Lozzi, L., et al., *Electronic structure of crystalline copper phthalocyanine.* The Journal of Chemical Physics, 2004. **121**(4): p. 1883-1889.
[25] Hoshino, A., Y. Takenaka, and H. Miyaji, *Redetermination of the crystal structure of α-copper phthalocyanine grown on KCl.* Structural Science, 2003. **59**(3): p. 393-403.
[26] Berger, O., et al., *Studies on phase transformations of Cu-phthalocyanine thin films.* Journal of Materials Science: Materials in Electronics, 2000. **11**(4): p. 331-346.
[27] Dufour, G., et al., *Copper phthalocyanine on Si(111)-7 × 7 and Si(001)-2 × 1 surfaces: an X-ray photoemission spectroscopy and synchrotron X-ray absorption spectroscopy study.* Surface Science, 1994. **319**(3): p. 251-266.
[28] Cruickshank, A.C., et al., *The Crystalline Structure of Copper Phthalocyanine Films on ZnO(1$\bar{1}$00).* Journal of the American Chemical Society, 2012. **134**(35): p. 14302-14305.
[29] Robertson, J.M., *136. An X-ray study of the structure of the phthalocyanines. Part I. The metal-free, nickel, copper, and platinum compounds.* Journal of the Chemical Society (Resumed), 1935: p. 615-621.
[30] Brown, C., *Crystal structure of β-copper phthalocyanine.* Journal of the Chemical Society A: Inorganic, Physical, Theoretical, 1968: p. 2488-2493.
[31] Cranston, R.R. and B.H. Lessard, *Metal phthalocyanines: thin-film formation, microstructure, and physical properties.* RSC Advances, 2021. **11**(35): p. 21716-21737.
[32] Afify, H.A., et al., *Effect of thermal annealing on the structural and optical properties of spin coated copper phthalocyanine thin films.* Journal of Molecular Structure, 2015. **1098**: p. 161-166.

[33] McAfee, T., et al., *Morphological, Optical, and Electronic Consequences of Coexisting Crystal Orientations in β-Copper Phthalocyanine Thin Films.* The Journal of Physical Chemistry C, 2016. **120**(33): p. 18616-18621.
[34] Patil, K.R., et al., *Copper phthalocyanine films deposited by liquid–liquid interface recrystallization technique (LLIRCT).* Journal of Colloid and Interface Science, 2007. **315**(2): p. 747-752.
[35] Kasha, M., H.R. Rawls, and M.A. El-Bayoumi, *The exciton model in molecular spectroscopy.* Pure and applied Chemistry, 1965. **11**(3-4): p. 371-392.
[36] Davydov, A.S., *The theory of molecular excitons.* Soviet Physics Uspekhi, 1964. **7**(2): p. 145-178.
[37] Szybowicz, M., et al., *High temperature study of FT-IR and Raman scattering spectra of vacuum deposited CuPc thin films.* Journal of Molecular Structure, 2004. **704**(1): p. 107-113.
[38] Achar, B.N. and K.S. Lokesh, *Studies on polymorphic modifications of copper phthalocyanine.* Journal of Solid State Chemistry, 2004. **177**(6): p. 1987-1993.
[39] Hoffmann, M., et al., *The lowest energy Frenkel and charge-transfer excitons in quasi-one-dimensional structures: application to MePTCDI and PTCDA crystals.* Chemical Physics, 2000. **258**(1): p. 73-96.
[40] Cudazzo, P., et al., *Frenkel versus charge-transfer exciton dispersion in molecular crystals.* Physical Review B, 2013. **88**(19): p. 195152.
[41] Bondarev, I.V., et al., *Lowest energy Frenkel and charge transfer exciton intermixing in one-dimensional copper phthalocyanine molecular lattice.* Applied Physics Letters, 2016. **109**(21): p. 213302.
[42] Knupfer, M., et al., *Mixing of Frenkel and charge transfer excitons in quasi-one-dimensional copper phthalocyanine molecular crystals.* Physical Review B, 2004. **69**(16): p. 165210.
[43] Liu, T., et al., *A generalized Stark effect electromodulation model for extracting excitonic properties in organic semiconductors.* Nat Commun, 2019. **10**(1): p. 5089.
[44] Huang, T.-H., *Electroabsorption Spectra of the Vanadyl Phthalocyanine Films.* Journal of the Physical Society of Japan, 1987. **56**(3): p. 1213-1222.
[45] Koch, M., et al., *Terahertz time-domain spectroscopy.* Nature Reviews Methods Primers, 2023. **3**(1): p. 48.
[46] Neu, J. and C.A. Schmuttenmaer, *Tutorial: An introduction to terahertz time domain spectroscopy (THz-TDS).* Journal of Applied Physics, 2018. **124**(23): p. 231101.
[47] Tóth, G., G. Polónyi, and J. Hebling, *Tilted pulse front pumping techniques for efficient terahertz pulse generation.* Light: Science & Applications, 2023. **12**(1): p. 256.
[48] Hebling, J., et al., *Generation of high-power terahertz pulses by tilted-pulse-front excitation and their application possibilities.* Journal of the Optical Society of America B, 2008. **25**(7): p. B6-B19.

[49] Hoffmann, M.C., et al., *Efficient terahertz generation by optical rectification at 1035 nm.* Optics Express, 2007. **15**(18): p. 11706-11713.
[50] Hebling, J., et al., *Velocity matching by pulse front tilting for large-area THz-pulse generation.* Optics Express, 2002. **10**(21): p. 1161-1166.
[51] Herter, A., et al., *Terahertz waveform synthesis in integrated thin-film lithium niobate platform.* Nature Communications, 2023. **14**(1): p. 11.
[52] Rasekh, P., et al., *Terahertz Nonlinear Spectroscopy of Water Vapor.* ACS Photonics, 2021. **8**(6): p. 1683-1688.
[53] Ryu, C. and S.G. Kong, *Atmospheric degradation correction of terahertz beams using multiscale signal restoration.* Applied Optics, 2010. **49**(5): p. 927-935.
[54] Kawase, K., et al., *THz imaging techniques for nondestructive inspections.* Comptes Rendus Physique, 2010. **11**(7): p. 510-518.
[55] Gallot, G. and D. Grischkowsky, *Electro-optic detection of terahertz radiation.* Journal of the Optical Society of America B, 1999. **16**(8): p. 1204-1212.
[56] Wu, Q. and X.C. Zhang, *Free-space electro-optic sampling of terahertz beams.* Applied Physics Letters, 1995. **67**(24): p. 3523-3525.
[57] Ibrahim, A., et al., *Ultra-high dynamic range electro-optic sampling for detecting millimeter and sub-millimeter radiation.* Scientific Reports, 2016. **6**(1): p. 23107.
[58] Heydarian, H., et al., *Adaptable electro-optic detection of THz radiation using a laser-written bull's-eye antenna.* Scientific Reports, 2025. **15**(1): p. 764.
[59] Heydarian, H., et al., *Enhanced nonlinear THz detection using a GaP photonic crystal waveguide and plasmonic antenna coupler.* APL Photonics, 2026. **11**(2): p. 026106.
[60] Bakker, H.J., et al., *Distortion of terahertz pulses in electro-optic sampling.* Journal of the Optical Society of America B, 1998. **15**(6): p. 1795-1801.
[61] Miller, D.A.B., et al., *Electric field dependence of optical absorption near the band gap of quantum-well structures.* Physical Review B, 1985. **32**(2): p. 1043-1060.
[62] Hulin, D. and M. Joffre, *Excitonic optical Stark redshift: The biexciton signature.* Physical Review Letters, 1990. **65**(27): p. 3425-3428.
[63] Malley, M., G. Feuer, and D. Mauzerall, *The stark effect in porphyrins.* Journal of Molecular Spectroscopy, 1968. **25**(4): p. 544-547.
[64] Yamanaka, T., K. Wakita, and K. Yokoyama. *Field-induced broadening of optical absorption in InP-based quantum wells with strong and weak quantum confinement*. in *Conference on Lasers and Electro-Optics*. 1994. Anaheim, California: Optica Publishing Group.
[65] Singh, P., et al., *Transient Terahertz Stark Effect: A Dynamic Probe of Electric Interactions in Polar Liquids.* J Phys Chem Lett, 2023. **14**(24): p. 5505-5510.
[66] Nakata, K., T. Kobayashi, and E. Tokunaga, *Mechanism for giant electro-optic response of porphyrin J-aggregates in polymer film and aqueous solution.* Optical Review, 2010. **17**(3): p. 346-351.

[67] Walters, G., et al., *The quantum-confined Stark effect in layered hybrid perovskites mediated by orientational polarizability of confined dipoles.* Nature Communications, 2018. **9**(1): p. 4214.
[68] Sari, E., et al., *Blue quantum electroabsorption modulators based on reversed quantum confined Stark effect with blueshift.* Applied Physics Letters, 2007. **90**(1): p. 011101.
[69] Hiraoka, T., et al., *Terahertz field effect in a two-dimensional semiconductor.* Nature Communications, 2025. **16**(1): p. 5235.
[70] Cunningham, P.D., et al., *Resonant optical Stark effect in monolayer WS2.* Nature Communications, 2019. **10**(1): p. 5539.
[71] Ghani, F., J. Kristen, and H. Riegler, *Solubility Properties of Unsubstituted Metal Phthalocyanines in Different Types of Solvents.* Journal of Chemical & Engineering Data, 2012. **57**(2): p. 439-449.
[72] Dyrda, G., et al., *Hydrogen bond-mediated conjugates involving lanthanide diphthalocyanines and trifluoroacetic acid (Lnpc2@ TFA): Structure, photoactivity, and stability.* Molecules, 2020. **25**(16): p. 3638.
[73] Ogunsipe, A.O., et al., *Protonation of some non-transition metal phthalocyanines—spectral and photophysicochemical consequences.* Journal of Porphyrins and Phthalocyanines, 2012. **16**(07n08): p. 885-894.
[74] Porotnikov, D., et al., *Photoinduced Rotation of Colloidal Semiconductor Nanocrystals in an Electric Field.* Nano Letters, 2021. **21**(11): p. 4787-4794.

Acknowledgments

This thesis would not have been possible without the guidance, support, and kindness of many people who have accompanied me throughout this journey. My deepest gratitude goes first to my advisor, Prof. Jiaojian (Tristan) Shi. His guidance, patience, and encouragement have shaped not only this work, but also my growth as a researcher. I am truly grateful for the opportunity to learn from his scientific insight, thoughtful advice, and dedication to research.

I am also sincerely thankful to my committee members, Prof. Dianne J. Xiao and Dr. Sharon Durfy, for their time, thoughtful feedback, and valuable suggestions. Their perspectives helped me think more deeply about my research and improved the quality of this thesis in many important ways.

My time in the Shi Lab has been meaningful because of both the research and the people around me. I am grateful to all members of the Shi Lab, including Kyan Ho, Yukun Li, Nathan Pringle, Isabel Sedwick, Chenyu Yang, and Weiwang Zeng, for their support, discussions, and companionship. I would especially like to thank Chenyu for his continuous help, encouragement, and friendship. His support, both scientifically and personally, has meant a great deal to me and has accompanied me through many important moments of my graduate study.

It has been a great privilege to study and work in the Department of Chemistry at the University of Washington. I feel very fortunate to have been part of such a supportive academic community, where I have grown not only as a student and researcher, but also as a person. During my time here, I also met many wonderful friends, including Kelly and Amy. Their kindness, friendship, and support brought warmth and joy to my graduate experience, and these memories will always remain precious to me.

Above all, my deepest love and gratitude belong to my parents. Their unconditional love, patience, and support have always been my greatest source of strength. Even from afar, their care and encouragement have given me the courage to face challenges and continue moving forward.

As this chapter comes to an end, I carry with me not only the knowledge and experience I have gained, but also the kindness, support, and beautiful memories given to me by the people around me. In the days ahead, I will continue to work hard and move forward with gratitude, carrying these warm wishes with me.